# Magmatism, serpentinization and life: Insights through drilling the Atlantis Massif (IODP Expedition 357)

Gretchen Früh-Green, Beth Orcutt, Stéphane Rouméjon, Marvin Lilley, Yuki Morono, Carol Cotterill, Sophie Green, Javier Escartin, Barbara John, Andrew Mccaig, et al.

**Article:**
Früh-Green, GL, Orcutt, BN, Rouméjon, S et al. (32 more authors) (2018) Magmatism, serpentinization and life: Insights through drilling the Atlantis Massif (IODP Expedition 357). Lithos, 323. pp. 137-155. ISSN 0024-4937

https://doi.org/10.1016/j.lithos.2018.09.012

# Magmatism, serpentinization and life: Insights through drilling the Atlantis Massif (IODP Expedition 357)

Gretchen L. Früh-Green[a,*], Beth N. Orcutt[b], Stéphane Rouméjon[a], Marvin D. Lilley[c], Yuki Morono[d], Carol Cotterill[e], Sophie Green[e], Javier Escartin[f], Barbara E. John[g], Andrew M. McCaig[h], Mathilde Cannat[f], Bénédicte Ménez[f], Esther M. Schwarzenbach[i], Morgan J. Williams[j,1], Sally Morgan[k], Susan Q. Lang[l], Matthew O. Schrenk[m], William J. Brazelton[n], Norikatsu Akizawa[o,2], Chiara Boschi[p], Kristina G. Dunkel[q], Marianne Quéméneur[r], Scott A. Whattam[s3], Lisa Mayhew[t], Michelle Harris[u,4], Gaye Bayrakci[u], Jan-Hinrich Behrmann[v], Emilio Herrero-Bervera[w], Kirsten Hesse[x], Hai-Quan Liu[y], Amila Sandaruwan Ratnayake[z,5], Katrina Twing[m,n], Dominique Weis[aa], Rui Zhao[ab], Laura Bilenker[aa]

[a] Institute of Geochemistry and Petrology, ETH Zurich, Clausiusstrasse 25, 8092 Zürich, Switzerland

[b] Bigelow Laboratory for Ocean Sciences, East Boothbay, ME, USA

[c] University of Washington, School of Oceanography, Seattle WA 98195, USA

[d] Japan Agency for Marine-Earth Science and Technology, Kochi Institute for Core Sample Research, Kochi, Japan

[e] ECORD Science Operator, British Geological Survey, Edinburgh EH14 4AP, UK

[f] Institut de Physique du Globe de Paris, CNRS, 1 rue Jussieu, 75238 Paris cedex 05, France

[g] University of Wyoming, Laramie WY 82071, USA

[h] University of Leeds, School of Earth and Environment, Leeds LS2 9JT, United Kingdom

[I] Institute of Geological Sciences, Freie Universität Berlin, Malteserstrasse 74-100, 12249 Berlin, Germany

[j] The Australian National University, Department Research School of Earth Sciences, Mills Rd, Acton, Australia. [1]Present address: CSIRO Mineral Resources, 26 Dick Perry Avenue, Kensington WA 6151, Australia

[k] ECORD Science Operator, Department of Geology, University of Leicester,University Road, Leicester LE1 7RH, United Kingdom

[l] University of South Carolina, 701 Sumter St. EWS 617, Columbia SC 29208, USA

[m] Michigan State University, 288 Farm Lane, East Lansing MI 48824,USA

[n] University of Utah, 257 South 1400 East, Salt Lake City, UT 84112-0840, USA

[o] Kanazawa University, Department of Earth Sciences, Kakuma Kanazawa, Ishikawa 920-1192 JAPAN. [2]Present address: Atmosphere and Ocean Research Institute, The University of Tokyo 5-1-5, Kashiwanoha, Kashiwa, Chiba 277-8564 Japan

[p] Institute of Geosciences and Earth Resources – CNR, Via Moruzzi 1, 56124 Pisa, Italy

[q] Physics of Geological Processes, University of Oslo, Sem Sælands vei 24, 0371 Oslo, Norway

[r] Mediterranean Institute of Oceanography (MIO), Aix Marseille Univ., Université de Toulon, CNRS, IRD, MIO UM 110, 13288, Marseille, France

[s] Korea University, Department Earth and Environmental Sciences, Seoul 136-701, Republic of Korea. Present address: Department of Geosciences, King Fahd University of Petroleum and Minerals, Dhahran 31261, Saudi Arabia

[t] University of Colorado – Boulder, 2200 Colorado Ave., Boulder CO 80466, USA

[u] University of Southampton, National Oceanography Centre, European Way, Southampton, SO14 3ZH, United Kingdom. [4] Present address: School of Geography, Earth and Environmental Sciences, 109 Fitzroy Building, Plymouth University, Plymouth PL4 8AA, United Kingdom

[v] GEOMAR Helmholtz Centre for Ocean Research Kiel, Wischhofstr. 1-3, 24148 Kiel, Germany

[w] University of Hawaii at Manoa, SOEST-Hawaii Institute of Geophysics and Planetology,1680 East West Road, Honolulu 96822, USA

[x] GeoZentrum Nordbayern, Friedrich-Alexander-University Erlangen-Nuremberg, Schlossgarten 5a, 91054 Erlangen, Germany

[y] Guangzhou Institute of Geochemistry, Chinese Academy of Sciences, Key Laboratory of Marginal Sea Geology, 511 Kehua Street, Tianhe, Guangzhou 510640, China

[z] Shimane University, Faculty of Science and Engineering, 1060 Nishikawatsu Matsue, Shimane 690-8504, Japan. [5]Present address: Mineral Resources and Technology, Faculty of Science and Technology, Uva Wellassa University, Passara Road, Badulla 90000, Sri Lanka

[aa] University of British Columbia, Earth, Ocean and Atmospheric Sciences, 2020-2207 Main Mall, Vancouver, BC V6T-1Z4, Canada

[ab] Centre for Geobiology, University of Bergen, Allegaten 4, 5007 Bergen, Norway

*Corresponding author: Gretchen L. Früh-Green at Institute of Geochemistry and Petrology, ETH Zurich, Clausiusstrasse 25, 8092 Zürich, Switzerland. Email address: frueh-green@erdw.ethz.ch

**Keywords**: IODP Expedition 357, Atlantis Massif, detachment faulting, serpentinization, Si metasomatism, deep biosphere

## 1. Introduction

It is now well recognized that slow spreading ridges are formed by interlinked processes of magmatism, asymmetric extension, and detachment faulting that result in the exposure and alteration of lower crustal and mantle-derived rocks in oceanic core complexes (OCCs) (Andreani et al., 2007; Boschi et al., 2006; Cannat, 1993; Früh-Green et al., 2004; Karson et al., 2006; Kelemen et al., 2007; Rouméjon et al, 2015). OCCs contain olivine-rich rocks that interact with seawater to produce serpentinite over a range of temperatures (Andreani et al., 2007; Boschi et al., 2006a; Boschi et al., 2006b; Cannat, 1993; Früh-Green et al., 2004; Karson et al., 2006; Kelemen et al., 2007; Rouméjon et al, 2015). Serpentinization is a fundamental process that controls rheologic and geophysical properties (Escartin et al, 2008; Schroeder et al, 2002) and is associated with the uptake or release of many major and minor components (Alt and Shanks, 2003; Boschi et al., 2008; Delacour et al., 2008; Früh-Green et al., 2004; Schwarzenbach et al., 2012). Serpentinization reactions also lead to highly reduced, alkaline (pH 9-12) fluids with high concentrations of hydrogen, methane and formate, and which have important consequences for long-term global geochemical fluxes and for biogeochemical cycles (Holm and Charlou, 2001; Konn et al., 2009; Lang et al., 2018; Proskurowski et al., 2006, 2008).

The Atlantis Massif (30°N, Mid-Atlantic Ridge) is one of the best-studied OCCs and hosts the off-axis Lost City hydrothermal field (LCHF) on its southern wall (Fig. 1). Serpentinization reactions in the underlying mantle rocks produce high pH (9-11), <91°C fluids that form large carbonate-brucite structures upon venting on the seafloor (Kelley et al., 2001, 2005; Ludwig, et al., 2006). The fluids have high concentrations of $H_2$, $CH_4$, $C_2$+ alkanes and formate ($HCOO^-$) that support novel microbial communities dominated by $CH_4$-cycling archaea in the

hydrothermal carbonate deposits (Brazelton et al., 2006; Brazelton and Baross, 2009; Lang et al., 2010; Méhay et al., 2013; Proskurowski et al., 2006, 2008; Schrenk et al., 2004). Formate and low molecular weight hydrocarbons in the Lost City hydrothermal vents are believed to be formed by abiogenic processes during serpentinization at depth (Lang et al., 2012, 2018; Proskurowski et al., 2008). Thus, the Atlantis Massif provides a natural laboratory to study the links between serpentinization processes and microbial activity in the shallow subsurface of ultramafic and mafic rock sequences that have been uplifted to the seafloor along a major detachment fault zone (Blackman et al., 2002; Cann et al., 1997; Boschi et al., 2006; Karson et al., 2006; Kelley et al., 2001, 2005; Schroeder and John, 2004). The processes controlling fluid flow and a deep biosphere are intimately linked; however, the spatial scale of lithologic variability, the implications for fluid flow paths and geochemical exchange, and the consequences for subsurface ecosystems supported by these systems remain poorly constrained.

Here we present an overview of Expedition 357 of the International Ocean Discovery Program (IODP), which cored seventeen shallow holes at nine sites (Figs. 1, 2) across the Atlantis Massif (Früh-Green et al, 2016). Expedition 357 was implemented by the ECORD Science Operator (ESO) as a Mission Specific Platform (MSP) expedition and consisted of an offshore phase on board the RRS James Cook in fall 2015 and a two-week onshore phase at the IODP Bremen Core Repository in January-February 2016 (Früh-Green et al., 2017a). A major aim of drilling was to investigate seawater infiltration and alteration processes, and their influence on the nature and distribution of microbial communities in lithologically heterogeneous domains of an oceanic core complex. Drilling along a spreading-parallel, east-west profile with seven sites targeted the serpentinite basement at varying distances away from the ridge axis and the Lost City vent field

(Fig. 1, Table 1; see also Früh-Green et al., 2015). Two sites were drilled on the eastern part of the southern wall (Sites M0068 and M0075), three sites in the central section north of Lost City (Sites M0069, M0072, and M0076), and two sites on the western end (Sites M0071 and M0073, with no recovery at M0073). This 8.5 km long profile allows us to explore the extent and activity of the subsurface biosphere in an actively serpentinizing environment and assess how abiotic and biotic processes change with aging of the lithosphere, variations in rock type, and with time of exposure on the seafloor. Two further shallow sites towards the central dome of the massif (Sites M0070 and M0074) targeted the mafic, plutonic domain drilled at IODP Site U1309. Penetration and core recovery were limited at these northern sites, and the recovered sequences were dominated by carbonate sediments and sedimentary breccias. The cores obtained during IODP Expedition 357 are the first continuous sequences of fault rocks recovered along a major detachment fault that has an inferred thickness of ~100 m (e.g., Karson et al., 2006; Schroeder and John, 2004). These cores provide a unique opportunity to study the interaction of magmatism, deformation and fluid-rock interaction during the evolution of the Atlantis Massif and the impact these processes on habitability for microorganisms.

## 2. Expedition strategy and methods

To obtain a comprehensive view of active serpentinization, fluid circulation and microbial activity, a strategy was developed based on the use of seabed drills that combined coring with water sampling and in situ geochemical measurements during drilling (Früh-Green et al., 2015). To enable continuous operations, two seabed drills were used: the British Geological Survey (BGS) RockDrill2 (RD2) and the Meeresboden-Bohrgerät 70 (MeBo) from the Center for Marine Environmental Sciences (MARUM; University of Bremen, Germany). This was the first

time that seabed drill technology was used in the ocean drilling program. Both drills are remotely operated systems that are lowered onto the seabed, with power and control maintained from the ship via an umbilical and using multiple rods and core barrels to progressively penetrate into the seabed (Früh-Green et al., 2017b). They are both based on an HQ-size, diamond coring system, producing between 61 and 62 mm diameter cores, similar in size to the standard IODP core diameter, while cutting a smaller diameter hole. By sitting on the seabed, they do not require heave compensation and consequently have good control on bit weight, analogous to land-based coring, and bottom seawater is used as the drilling fluid.

The expedition included engineering developments that allowed continuous measurement of geochemical parameters during drilling, sampling of bottom water after drilling, and the injection of synthetic contamination tracers during drilling. To evaluate the composition of fluids emanating from the flushed boreholes in real-time, a suite of in situ sensors mounted on the drills measured dissolved oxygen, hydrogen and methane, temperature, pH, and oxidation-reduction potential (ORP) during coring operations. Bottom water was collected prior to drilling using the ship's CTD Niskin bottle rosette and after drilling using Niskin bottles mounted on the drills. Each rock drill was also equipped with a pump system to deliver perfluoromethylcyclohexane (PFC) tracer during drilling to assess seawater contamination of the cores (Orcutt et al., 2017). Shipboard sampling also evaluated contamination potential of the drilling equipment itself, including greases and other lubricants. When recovered to deck, water samples were immediately collected for dissolved $H_2$ and $CH_4$ concentration analyses, cell counts and PFC tracer, which were measured onboard, and subsamples were taken for shore-based geochemical and microbiological analyses (see Früh-Green et al., 2017b). Borehole plug systems were also

designed to enable future sampling of borehole fluids; these were installed at Holes M0072B and M0075B (Früh-Green et al., 2017b). These will be visited on a US-led research expedition in September 2018 with the ROV Jason (funded by the National Science Foundation) to further investigate the serpentinization and microbiological processes operating in this system.

To accomplish the microbiology related objectives of the expedition and to enable preservation of ephemeral microbiological properties, whole round core (WRC) samples were collected shipboard immediately after core retrieval, curation, and scanning with the multi-sensor core logger. In total, 42 WRC samples were taken from the 17 holes drilled during the offshore phase of the expedition, yielding nearly 8 m in total length and representing ~14% of the entire core recovered. For part of these WRCs, potentially contaminated exterior surfaces were flame-sterilized on the ship in a KOACH open clean system with care to avoid potential contaminants (e.g. dust). Interior pieces of rock were collected after crushing using a flame-sterilized chisel and fixed for microbial cell detection (Früh-Green et al., 2017b). Subsamples of WRCs were used to establish 29 different enrichment experiments on the ship, with initial indications of positive activity in some of the treatments based on elevated cell counts. Remaining portions of the WRCs were immediately frozen at -80°C and shipped to the Kochi Core Center, Japan, at the end of the offshore phase. There, exteriors of the WRCs were removed under sterile conditions with a band saw system equipped in a clean booth (Orcutt et al., 2017) and the WRC interiors and exteriors were subsampled for multiple shore-based analyses.

Taking advantage of weather and operational downtime, IODP Expedition 357 generated a high-resolution multibeam bathymetry map across the Atlantis Massif. The new bathymetry, after

185 processing, provides a grid with a resolution of 20–50 m, which is two to five times higher
186 resolution than previously available bathymetry for this area (100 m) (Blackman et al., 2002).
187 The survey covered the entire striated detachment fault surface of the Atlantis Massif and
188 surrounding terrain, which included the ridge axis to the east, the Atlantis Fracture Zone to the
189 south, the tectonized terrain off-axis and west of the detachment, and its gradual narrowing
190 transition to the adjacent seafloor to the north (Fig. 1).
191
192 As with all IODP mission-specific platform expeditions, no cores were split during the offshore
193 phase. A comprehensive onshore phase at the IODP Bremen Core Repository complemented the
194 offshore phase, during which the cores were described in detail and the IODP minimum and
195 some standard measurements were made (see Früh-Green et al., 2017b for details). Bulk rock
196 preparation and geochemical analyses deviated from standard IODP procedure and were
197 conducted in the ultraclean laboratories of the Pacific Centre for Isotopic and Geochemical
198 Research at the University of British Columbia (Canada). Major elements were measured using
199 an inductively coupled plasma-optical emission spectrometer (ICP-OES) and trace elements
200 (including Cr and Ni) were determined with a high-resolution inductively coupled plasma-mass
201 spectrometer (HR-ICP-MS), using international standards and an in-house standard (see
202 Geochemisty section in Früh-Green et al., 2017b).
203

## 3. Expedition highlights

In brief, comparison of the recovered rock types (Fig. 2), cross-cutting relationships and the newly produced bathymetric map (Fig. 1) indicate that the central sites recovered in situ sequences that provide a record of (from oldest to youngest): early magmatism emplaced in the shallow mantle, multiphase progressive seawater penetration, serpentinization and metasomatism, dolerite intrusions, and recent basaltic volcanism. As the boreholes were located across the detachment fault zone, the cores likely sampled different structural levels which were tectonically transposed over the thickness of the detachment fault zone (~100 m). The two eastern Sites M0075 and M0068 and the western Site M0071 recovered fault scarp deposits. The scarp deposits and rubble intervals provide no information as to the orientation of structures or veins; however, the rock types, deformation and alteration characteristics, as well as contact relationships preserved in coherent portions of the cores, are similar to those recovered in the in situ sequences at the central sites and provide information about the magmatic, metamorphic and deformation history at shallow levels of the detachment fault zone. Sedimentary breccias with variably rounded clasts (predominantly basalt with some serpentinite, gabbro, and dolerite) in a foraminiferous carbonate matrix were recovered at Site M0070 to the north of the east-west transect, and only one short highly disturbed sediment core was recovered from Site M0074.

### 3.1 Multibeam bathymetry

New bathymetric mapping revealed a striated detachment surface with variations in geometry along-axis from south to north (Fig. 1a). Near the transform wall, the detachment fault surface summits near the Lost City hydrothermal field at <800 meters below sea level (mbsl); from there it dips ~8° east toward the ridge axis, ~6° to the west, and ~8°–10° to the north toward the

central dome. The detachment deepens to the north to >1500 mbsl. This deepening is associated with a change in shape; the detachment shows curvature along the spreading direction with slopes of up to 15° at its termination toward the ridge axis, becomes subhorizontal, and dips up to 10° away from the axis.

The hanging wall cutoff (termination) is well preserved toward the northern, deeper part of Atlantis Massif, corresponding to a sharp contact between the ridgeward-dipping striated fault plane and the adjacent seafloor volcanic terrain. This volcanic terrain has a <10° tilt westward, away from the ridge axis, and hosts volcanic cones and a bathymetric texture typical of volcanic terrain along the rift valley floor (Fig. 1b). This portion of volcanic seafloor is bound further east by a fault scarp and corresponds to the top of a back-tilted tectonic block, as previously identified (Blackman et al., 2002; Cann et al., 1997).

The termination is not preserved to the south, ridgeward of the elevated portion of the detachment. Instead, the striated surface is dissected by a major scarp, with a relief of up to 3000 m from the rift valley floor and the top of the scarp. This scarp shows a lobate structure indicating mass-wasting processes (slumping). Laterally, it links north with the fault scarp bounding the tectonically uplifted volcanic seafloor, which corresponds to the present-day rift valley wall fault. The striated surface is also affected by extensive mass wasting along its southern boundary toward the transform valley (Fig. 1b). The mass wasting produces scarps that are concave at their subvertical headwall. The transform wall south of Atlantis Massif has an average slope of ~20° and numerous channels bound by high ridges channelling debris at the base of the transform valley. Widespread mass wasting at smaller scales is also observed on

steeper slopes of the detachment fault surface along the flanks of larger-scale striations. Late small-slip faults (centimeters to tens of meters) cut the striated detachment surface and are subparallel to oblique to the ridge axis. Most have scarps facing away from the ridge axis, with scarps up to ~10–20 m in vertical relief and which have irregular traces.

## 3.2 Lithology, alteration, and structure

### 3.2.1. Lithology

More than 57 m of core were recovered, with borehole penetration depths ranging from 1.3 to 16.44 meters below seafloor (mbsf). Core recoveries ranged from 23 to 75% of total penetration, with 100% recovery in some intervals (Table 1; Figure 2). This significant recovery of exhumed mantle peridotite at the surface of a major detachment fault zone is unprecedented in the history of ocean drilling and provides a new window into understanding interlinked processes of crustal accretion, deformation and alteration that to date could not be deduced with conventional rotary drilling, dredging or submersible sampling. Many lithologic and intrusive contacts, deformation features and alteration characteristics are preserved in the cores, even in highly fractured and/or sheared intervals. The cores highlight a highly heterogeneous lateral and vertical distribution of ultramafic and mafic rocks that host a range of alteration styles and extent of deformation (Figs. 2 and 3).

Of the core recovered from the six sites across the southern wall (from west to east: M0071, M0072, M0069, M0076, M0068, M0075; Figs. 1a and 2), serpentinized harzburgite and dunite make up 44% of the core by length. Other major rock types include basaltic rocks and metadolerites (combined 24%) and schistose metasomatic rocks with varying proportions of talc,

amphibole and chlorite (11%). Minor lithologies include calcareous sedimentary units (8%), and gabbroic rocks (4%). In comparison, previous dredging and Alvin dive campaigns at the southern Atlantis Massif recovered a similar percentage of ultramafic rocks (45% of total samples collected), but a higher percentage of gabbroic rocks (24%), metasomatic rocks (22%) and sediments (15%), and less basaltic and doleritic rocks (5%) (Schroeder and John, 2004; Boschi et al., 2006a; Karson et al, 2006). The proportion of gabbro to peridotite was less than at IODP Site U1309, where 1408m of gabbroic rocks were recovered; however, the proportion of dolerite was comparable (Blackman et al., 2006; McCaig and Harris, 2012). A synthesis of the lithological contacts, mineralogies and off shore analyses of the key sites are given in Appendixes A through J.

The ultramafic rocks are dominated by harzburgites punctuated by intervals of dunite and minor pyroxenite veins. Gabbroic rocks occur locally as zones of melt impregnation (tens of centimeters thick) and veins at Sites M0068, M0071, M0072 and M0076 (Fig. 2). The harzburgites and dunites exhibit protogranular textures and are extensively serpentinized. Intervals of weakly porphyroclastic serpentinized peridotites were rare and localized. Serpentinized dunites are found exclusively as discrete intervals alternating with harzburgite and likely represent relict mantle melt channels or domains of melt-rock interaction (Kelemen et al., 1992; Nicolas, 1986). Mantle melt-rock reaction textures including vermicular to subhedral spinels (e.g., Nicolas and Prinzhofer, 1983) and pyroxene veins were also observed. The distribution of gabbro rocks is highly heterogeneous downhole and there was an absence of continuous, coherent sections of gabbroic core. Rare magmatic fabrics characterized by diffuse but planar centimeter-scale banding/layering of igneous minerals in gabbroic rocks were

296 recovered in Hole M0068B. Dolerite intrusions, basaltic rocks and local domains of
297 hyaloclastites represent the latest stage of magmatic activity. Metamorphosed dolerite intrusions
298 ranging from a few cm to several meters in thickness were recovered at the central and eastern
299 sites, and some dolerite intervals in Hole M0075B show chilled margins against fault rocks (see
300 Fig. F5 in Früh-Green et al., 2017c). Dolerites and metadolerites as well as poorly vesicular
301 aphanitic to microcrystalline basalts with glassy margins also occur as mm-dm sized components
302 within the sedimentary breccias. The dolerites were variably altered, while basalts were often
303 fresh, with no sign of metamorphism.
304
305 All types of variably altered and deformed ultramafic and mafic rocks occur as clasts in
306 sedimentary breccias overlying the basement sequences and as fault scarp deposits. The
307 sedimentary cap rocks include basaltic breccias with foraminiferous carbonate sand and/or
308 lithified foraminiferous carbonate matrix. Fresh and partially palagonitized glass in basaltic
309 components and hyaloclastites were observed in some of the breccias and in some cores
310 containing carbonate sediment.
311
312 3.2.2 Serpentinization and metasomatism
313 The IODP Expedition 357 cores reveal a high degree of alteration and intervals with variable
314 metasomatic overprinting in the ultramafic rocks. Different types of alteration are distinguished
315 depending on protolith: serpentinization, talc-amphibole-chlorite metasomatism and oxidation in
316 the ultramafic rocks; and hydration, oxidation, and local Ca-metasomatism/chloritization along
317 contacts between doleritic and gabbroic domains and serpentinites. The sequence of alteration

textures and the associated mineralogical assemblages vary between sites and downhole in some cases (Früh-Green et al., 2017c, d,e and f).

Serpentinization is common in the ultramafic rocks at all sites and occurs as pervasive alteration with extensive to complete replacement of the primary mineralogy, forming mesh textures after olivine, bastites (lizardite ± chrysotile) after orthopyroxene, and different generations of serpentine veins (Fig. 4). A detailed study of the textures and mineralogies of the serpentinized serpentinites combined with in situ major and trace element analyses in primary phases and serpentine minerals is given in Rouméjon et al. (2018). These are used to make a model for the development of alteration heterogeneities at the Atlantis Massif and are summarized briefly here. Hydration of olivine led to a typical serpentine mesh texture, which is characterized by mesh cells, tens to hundreds of microns in size, delimited by microfractures that initially crosscut the olivine. Lizardite mesh rims form the outer part of cells, whereas the mesh cores are made up of poorly crystallized lizardite and/or chrysotile. Magnetite tends to crystallize in the mesh rims and concentrates along microfractures. Progressive fluid infiltration and serpentinization is evident by recrystallization of mesh textures to chrysotile-polygonal serpentine or antigorite, and by multiple sets of veins with variable infillings (Fig. 4; see also Rouméjon et al., 2018). The orthopyroxenes also show overprinting relationships with replacement by serpentine, talc, tremolite and/or chlorite.

Although the depth of penetration was limited, the abundance of gabbroic intrusions appears to increase from west to east and is associated with talc-amphibole-chlorite metasomatism and in some cases chlorite blackwall formation. Multiple generations of amphibole are observed in the

gabbroic domains, reflecting progressive alteration from amphibolite to greenschist-facies conditions during exhumation, as described in previous studies (Schroeder and John, 2004; Boschi et al., 2006a). Metasomatism is characterized by varying proportions of talc, chlorite and tremolitic amphibole and is a common feature at the central and eastern sites, evident as pale greenish-white domains or vein networks (Figs. 3b and d). Talc-metasomatism is rare at the western Site M0071 and is most prevalent in Hole M0072B near Lost City (Fig. 2). It develops both as pervasive, irregular patches in the serpentinites or as localized alteration associated with mafic intervals, enclosing serpentinized harzburgite on centimeter to decimeter scales (Figs. 5 and 6). The metasomatic domains are locally deformed and the talc-rich zones are commonly sheared, forming intervals of talc-amphibole-chlorite schists. Talc generally replaces mesh textures or forms in veins in the serpentinites, whereas tremolitic amphibole and chlorite assemblages are found in mafic domains and at contacts between serpentinite and gabbro or metagabbro, or in domains that have been infiltrated by mafic melts (Figs. 5 and 6). In some sections, amphibole and chlorite appear to have formed prior to talc. Relict olivine is also found in a number of cores in the central and eastern sites (Holes M0068, M0072, M0076) where talc-amphibole-chlorite metasomatism and/or chlorite-rich alteration is most prevalent.

Metasomatism is particularly pronounced in Hole M0072B, where complex zoned intervals (approximately 5 cm thick) with mafic lenses adjacent to chlorite-rich blackwalls are repeatedly present over a few meters. Exceptional relationships between mafic intrusions (possibly doleritic or microgabbro), talc ± amphibole ± chlorite zones, and serpentinized dunite and harzburgite are observed in Cores M0072B-6R1 (Fig. 5d) and M0072B-7R1 (Fig. 6). The mafic intrusions in these cores have pale brown to pinkish-brown central domains that are surrounded by external

364 dark green domains made up mostly of chlorite (chlorite blackwall), which in turn grade into
365 talc-amphibole-rich domains at the contact to the serpentinites. The pinkish brown domains were
366 originally described as rodingites (Früh-Green et al., 2017d), which have been found during
367 previous sampling campaigns along the southern wall of the Atlantis Massif (Boschi et al.,
368 2006a). However, subsequent analyses have yet to identify typical Ca-Al silicates, such as
369 epidote (clinozoisite), diopside, prehnite, (hydro)garnet or vesuvianite, which are commonly
370 found in rodingites in similar associations with serpentinites. Instead, preliminary X-ray
371 diffraction (XRD), micro-Raman spectroscopy and microprobe analyses (unpublished data)
372 indicate that these zones are indeed Ca-rich but are made up of chlorite and fine-grained
373 aggregates of anorthite ± tremolitic and/or pargasitic amphibole. The association of chlorite and
374 anorthite in these domains could result from higher temperatures of alteration than are typically
375 associated with rodingite (> ~350°C). Anorthite may also form from fluids with higher $CO_2$
376 concentrations (Rice, 1983).
377
378 Although brucite occurs in the actively venting carbonate structures at Lost City (Kelley et al.,
379 2001; Früh-Green et al., 2003; Ludwig et al., 2006) and is a common product of serpentinization
380 reactions, it has not been found in previous studies of the basement rocks of the Atlantis Massif
381 (e.g., Boschi et al., 2006a; 2008). In the IODP Expedition 357 cores, brucite could not be
382 detected visually, microscopically or with XRD on bulk rock samples (Früh-Green et al.,
383 2017c,d,e). In addition, a brucite signature is absent in micro-Raman spectra, which together
384 with nearly stoichiometric serpentine compositions of the mesh texture serpentine minerals
385 (Rouméjon et al., 2018; Rouméjon et al., this issue) strongly suggest that brucite is absent in the
386 serpentinized peridotites that make up the southern wall of the Atlantis Massif. The absence (or

dissolution) of brucite and abundance of talc in the metasomatic assemblages may be a consequence of high Si activities in the fluids during progressive hydrothermal alteration along the detachment fault zone and/or high alteration temperatures (above 350°C) during denudation of the mantle.

Finally, later-stage oxidation of the serpentinized harzburgites and dunites is characterized by reddish to brown alteration, occurring as both pervasive and localized features, and is commonly associated with calcium carbonate veins (Fig. 3a). Overprinting relationships in the ultramafic rocks demonstrate an overall progression from local amphibole-chlorite alteration to serpentinization to talc ±amphibole ±chlorite metasomatism and later oxidation.

Hydration of the dolerites and basalts manifests as pervasive background alteration with moderate to high intensity accompanied by alteration halos that flank veins. Secondary minerals vary depending on the temperature of alteration, with dolerites dominated by greenschist-facies minerals (chlorite, amphibole, and epidote), and basalts by low-temperature oxidation to iron oxyhydroxides and clays. Epidote occurs as a dominant vein mineral in metadolerites in Hole M0069A often with vein halos dominated by chlorite. Chilled margins in dolerite dikes that have intruded into talc-amphibole-chlorite schists are observed at the most eastern Site M0075. Hydration of gabbros is generally associated with chlorite-amphibole assemblages.

Hydrothermal veins are present in all rock types. Vein minerals include serpentine, talc, chlorite, amphibole, epidote, quartz, and calcium carbonate. The veins are often complex, with multiple infillings and internal textures, highlighting a protracted formation history. Crosscutting

relationships are also complex, with the same veins observed both crosscutting and being crosscut by a second vein type. The occurrence of calcium carbonate veins was surprisingly limited in the recovered cores. Carbonate veins are more prevalent in the sites around the Lost City hydrothermal field, where they occur mostly within entirely serpentinized dunites and harzburgites. At the western Site M0071, calcium carbonate veins in the serpentinites predate fractures that are infilled with foraminiferous carbonate sand (Fig 3a), suggesting open fractures at the top of the detachment fault zone, as described by Schroeder et al. (2002) based on Alvin dive samples.

3.2.3 Structures and deformation history

The drilled sites are located along a roughly spreading-parallel, 8.5 km transect (west–east) in various positions (trough or wall/flank) relative to individual corrugations of the detachment fault over the southern wall of Atlantis Massif (Fig. 1). Despite the fact that a number of the holes recovered rocks that are considered not to be in situ, generalizations can be made about the structural history recorded (Früh-Green et al., 2017c,d,e,f). As in IODP Hole U1309D at the central dome of the Atlantis Massif (Blackman et al., 2006), strongly deformed microstructures formed at high temperatures are rare in the IODP Expedition 357 cores. The majority of the recovered cores show amphibolite- to greenschist-facies, semibrittle and brittle deformation (Figs. 3 and 6), which contrasts with previous studies of samples recovered by submersible and by dredging that document higher temperature, high strain conditions in parts of the southern wall of the massif (Boschi et al., 2006a; Karson et al., 2006; Schroeder and John, 2004). Fault rocks in shear zones preserved in the cores are dominated by anastomosing intervals of variable intensity, with schistose amphibole ± talc ± chlorite zones up to tens of centimeters thick. The

schistose shear zones contain undeformed dolerite intrusions with preserved chilled margins; elsewhere, dolerite sheets record brittle and semibrittle deformation textures indicating repeated magmatism and faulting. Extensive intervals of flattened breccia are associated with dolerites but often contain clasts of fault rocks derived from other lithologies. Some breccia clasts show relicts of higher temperature amphibolite facies deformation, as do serpentinized intervals in the margins of talc-tremolite-chlorite schist zones. Intense cataclastic intervals and possible fault gouge occur within some breccias and also as thin intervals within the schistose shear zones. Discrete fault planes occur in most cores with a range of orientations, but lineations are generally shallow on both steep and shallow fault planes. An important observation is that the serpentinites are almost invariably statically altered, with no schistose serpentine developed and only occasional cataclastic seams. Strain within serpentinite intervals seems to be almost entirely localized within metasomatic talc-tremolite-chlorite horizons.

### 3.3 Bulk rock geochemistry

A wide range of major and trace element bulk rock compositions reflect the differences in rock type as well as the type and extent of alteration (Table 2, Figs. 7, 8 and 9). Independent of site location, the talc-amphibole-chlorite schists typically have high $SiO_2$ contents, ranging from 50-60 wt%, and low $MgO/SiO_2$ ratios (0.45 – 0.51) as well as lower loss on ignition (LOI: 4.3 – 5.3 wt%) than the serpentinites (LOI: 11.95 – 13.8 wt%). The serpentinized ultramafic rocks have the highest $MgO/SiO_2$ ratios (0.96 – 1.19) and variable but high Cr (up to 29,698 ppm in Hole M0069) and Ni (up to 14,590 ppm in Hole M0071A) contents. Overall, the talc-amphibole-chlorite schists (and in some cases the impregnated/metasomatized ultramafic rocks) are richer in $Al_2O_3$, $Na_2O$, CaO, $TiO_2$, and depleted in $Fe_2O_3$ (Fig. 7). The talc schists are also enriched in Cr

456 and Ni relative to the gabbroic rocks and dolerites but have lower concentrations than the
457 ultramafic lithologies (Fig. 8). Samples from Hole M0068B exhibit the highest $SiO_2$, CaO, and
458 $Na_2O$ contents, but the lowest $Al_2O_3$ and $Fe_2O_3$ contents. The most altered dolerites and gabbros
459 have characteristically low $SiO_2$ concentrations (26.2 – 31.6 wt%), high $Fe_2O_3$ (18.8 –32.1 wt%)
460 and low Ni and Cr (Fig. 8), which reflects the high modal abundance of chlorite in these rocks
461 and suggests Si mobility and loss during alteration (Fig. 9). The Mg and Ni concentrations of the
462 IODP Expedition 357 serpentinites and impregnated serpentinites are higher than those
463 recovered during IODP Expeditions 304-305 and likely reflects the more primitive nature of the
464 mantle peridotites recovered along the southern wall. The gabbroic compositions are similar to
465 the IODP Hole U1309D gabbros, but the dolerites and metadolerites have higher Ni
466 concentrations and may be the result of a higher primary modal abundance of olivine (Fig. 9).
467
468 The Rare Earth Element (REE) patterns group by lithology and show a weakly defined
469 enrichment from west to east (Fig. 10) and some variations downhole. The serpentinized
470 ultramafic rocks have relatively flat to slightly light REE (LREE) depleted chondrite-normalized
471 patterns (i.e., typically centered around 1 or below). The impregnated/metasomatized
472 serpentinites from Hole M0072B exhibit values slightly higher than 1. Dolerites and gabbros
473 exhibit moderate LREE depletions with values ranging between 1 and 10. Two of the talc-
474 amphibole-chlorite schists have REE patterns resembling the impregnated/metasomatized
475 samples. Positive and negative europium anomalies were observed but do not correlate with a
476 particular lithology or site. Along with correlated Mg# and Ni abundances (Fig. 8), geochemical
477 trends in the serpentinized ultramafic rocks include a common uranium positive anomaly (the
478 intensity of which decreases in impregnated / metasomatized samples) (Früh-Green et al.,

2017c,d,e) and enriched lithium, cerium, and strontium anomalies in the central sites (Table 2). Such anomalies are commonly related to alteration processes, either from hydrothermal alteration or from late interaction with seawater on the seafloor. Rouméjon et al. (2018) document regional trends in trace and REE element compositions in serpentine minerals compared to primary olivine and attribute the regional and downhole variations to mobilization of elements during the successive stages of exhumation as a result of early melt emplacement, serpentinization-related fluid-rock interaction, and later fluid-rock interaction. LREE enrichments due to the proximity with metagabbros or metadolerites are particularly observed in samples from Holes M0068B and M0072B (see also Boschi et al, 2006a) and contribute to the downhole variations.

### 3.4 Volatile concentrations

Elevated bottom water gas concentrations recorded by the sensor package and water sampling confirmed that serpentinization is on-going at the Atlantis Massif (Figs. 11 and 12). Water samples before and after drilling indicated "hot spots" of dissolved hydrogen over Sites M0068, M0072, M0069, M0070 and M0071, with the highest concentrations of 323 nM measured in Hole M0072B. Elevated concentrations of methane were found over Sites M0072, M0070, and M0071 (Fig. 11, Table 1; see also Table T12 in Früh-Green et al., 2017c). A CTD cast directly over the Lost City hydrothermal vents (Site M0072) just south of the central drill sites had significantly elevated methane and hydrogen (35–48 nM and 196–267 nM, respectively). On a regional scale, hydrogen concentrations tended to be highest in the central sites and at the eastern Site M0068, which may reflect active serpentinization in the vicinity of the Lost City hydrothermal field (Fig. 11; Table 1). However, the interpretation of the regional-scale influence

502 on methane and hydrogen fluxes out of the basement is ambiguous since the depth of penetration
503 into the basement was limited to <20 mbsf.
504
505 In addition to elevated dissolved gas concentrations measured in the fluids, gas bubbles were
506 observed issuing from the hole and around the drill base during operations at Site M0070, even
507 when coring had stopped (Fig. 13). The bubbles could not be sampled directly with the seabed
508 drills and thus their composition remains unknown. Bathymetry indicates that Site M0070 lies
509 west of the western limit of the preserved striated detachment surface of Atlantis Massif (Fig. 1)
510 at the foot of a ~30 m high irregular mound (Figure F2A in Früh-Green et al., 2017f). The three
511 holes penetrated the same structural unit composed of either loose or cemented basalt clasts with
512 vesicles and glass within a carbonate matrix. The mound is likely a volcanic cone that has
513 undergone faulting and/or mass wasting and, thus, we cannot exclude volcanic gases as a source
514 of the bubbles observed at this site.
515
516 In addition to the water sampling observations, the drill-mounted sensors recorded peaks in
517 methane and pH that correlated with sharp decreases in oxidation-reduction potential (ORP) at
518 many sites (Figure 12, Früh-Green et al., 2017c,d,e,f). Low ORP (or Eh) reflects reducing
519 conditions and can be interpreted as elevated hydrogen concentrations and/or other reduced
520 components (such as reduced iron and hydrogen sulphide) in the fluid. The ORP sensor does not
521 respond to methane. In some cases, excursions in the sensor signals were observed while
522 drilling, which suggests that horizons that were penetrated released reduced basement fluids and
523 volatiles into the drilling fluid. In other cases, we observed variations in the methane, pH and
524 ORP signals even when no drilling operations were underway or when the drills touched down

on the seabed, suggesting that diffuse reduced fluids may be present at the top of the massif. In many cases we observed strong negative spikes in the ORP signals without a corresponding methane signal, which points to hydrogen and/ or other reduced phases being released into the drilling fluids. Due to limited core recovery, we were not able to clearly correlate the excursions in sensor data with specific horizons or rock types. On a regional scale, negative spikes in ORP were observed in most of the holes in the central sites, which is consistent with the higher dissolved $H_2$ and $CH_4$ concentrations at these sites and may reflect hydrothermal circulation related to the Lost City hydrothermal field.

It is worth noting that the dissolved methane concentrations were monitored with a Franatech METS sensor. Post-cruise evaluation of this sensor revealed that it responds to both $CH_4$ and $H_2$ with a response factor of 1 to 0.02, respectively. This complicates interpretations of the output of this sensor because $H_2$ concentrations typically exceed those of $CH_4$ in this environment. For example, in Lost City hydrothermal fluids, the $H_2/CH_4$ ratio varies from 0.5 to 9.2 (Proskurowski et al, 2008). Where we measured bottom water concentrations from CTD casts, $CH_4$ was often below our detection limit (0.7 nM); however, at some sites both $H_2$ and $CH_4$ were present and the $H_2/CH_4$ ratio ranged from 5.5 to 20.9. In samples taken in the Lost City plume, the average ratio was 5.3. Samples from the drill-mounted Niskin bottles yielded $H_2/CH_4$ ratios ranging from 1.2 at Site M0070A to 167 at Site M0068B (see Table T12 in Früh-Green et al., 2017c). Although we were unable to make quantitative estimates of volatile concentrations from the sensor data, the METS sensor likely recorded both $H_2$ and $CH_4$, and it is possible that the output values we observe represent $H_2$ concentrations that are a factor of 50 times higher than the actual recorded

values given as $CH_4$ concentrations. Horizons with high $H_2$ concentrations are also indicated by the fact that elevated $CH_4$ signals often correlated with strong decreases in ORP.

### 3.5 Microbiology sampling

To accomplish the microbiology-related objectives of the expedition, an extensive program was carried out on board the ship to collect whole-round core samples immediately after core retrieval, curation, and scanning with the multisensor core logger to enable preservation of ephemeral microbiological properties. This program included (1) frozen preservation of core material for DNA- and lipid-based analyses in shore-based laboratories, (2) establishment of enrichment incubations on the ship (at ambient or in situ pressure) to assess the potential for various microbial metabolisms, (3) collection of samples to evaluate the performance of the contaminant tracer delivery, (4) preservation of samples for biomass determination via cell counting, and (5) collection of parallel samples for spatial and isotopic geochemical determination, particularly focused on carbon and minerals.

A major technical development for this expedition to enable microbiological analysis was establishing the delivery system for adding a synthetic tracer (PFC) into the drilling fluids to monitor the possibility of drilling-induced contamination (Orcutt et al., 2017). Samples of core barrel liner fluids, sensor package Niskin bottles, and exterior and interior pieces of whole-round core were collected to quantify the concentration of PFC tracer added during drilling operations and track its potential distribution into samples. After overcoming some technical difficulties with the metering pump in the delivery system, we established that PFC was delivered at saturating (>1 mg/L) concentrations into the drilling fluids (Orcutt et al., 2017). Moreover,

appropriate handling conditions combined with coherent core samples resulted in the absence of tracer from the interior of core samples (whereas less coherent materials suffered potential contamination from intrusion of tracer). Overall, implementation of the tracer injection system for seabed drill systems proved to work, and PFC concentrations on the exterior and interior of core samples could be used as a measure to assess the quality of the sample material for detailed microbiological and geochemical analyses (Orcutt et al., 2017).

To obtain an initial assessment of microbial biomass in the core samples, cell abundance was determined on the ship and onshore at the Kochi Core Center (Japan) in an ultraclean laboratory. Direct counting was made with an epifluorescence microscope following cell separation from flame sterilized interior portions of subsamples. To enable low levels of cell detection, great care was taken onshore and offshore to minimize contamination of samples (Früh-Green et al., 2017b; Morono et al., 2017), resulting in a limit of detection of 9.8 cells $cm^{-3}$. Cell abundance in the core samples was variable and relatively low, ranging from tens to thousands of cells/$cm^3$, with many of the basement samples often below the minimum quantification limit of 9.8 cells $cm^{-3}$ (Fig. 14). Cell counts in the interior portions of the basement rocks ranged from <10 to 6.5 x $10^2$ cells $cm^{-3}$, with one sample from Hole M0071A yielding 4.1 x $10^3$ cells $cm^{-3}$. Excluding the short core obtained at Site M0074 (because of contamination issues with core handling), the highest cell counts were found in the sediments in Hole M0069A near the contact to the basement, reaching up to 1.6 x $10^4$ cells $cm^{-3}$ at 5.46 mbsf, and decreased rapidly to <$10^2$ cells $cm^{-3}$ in the underlying basement rocks. The deepest samples were from this hole (at 14.6 mbsf), where 10-24 cells $cm^{-3}$ were measured in the serpentinites. A similar trend was observed at Hole

M0072B, with up to 5 x$10^2$ cells $cm^{-3}$ within the top meter of the hole and decreasing to <20 cells $cm^{-3}$ below 6.5 mbsf (Fig. 14).

The cell densities in the IODP Expedition 357 drill cores are distinctly lower than in the actively venting Lost City carbonate towers ($10^7$ to $10^8$ per gram of wet weight; Kelley et al., 2005). They are also low in comparison to cell densities in fluids sampled in actively serpentinizing environments on land, which are typically less than $10^5$ cells $ml^{-1}$, and as low as $10^2$ cells $mL^{-1}$, although continental sites of serpentinization represent different niches within the subsurface ecosystem (e.g., Schrenk et al., 2013; Brazelton et al., 2017). These cell densities are also lower than in mafic subseafloor cores, which have been estimated at ~$10^4$ cells per gram of rock (Jørgensen and Zhao, 2016). Overall, the strict sampling handling protocols allowed for very low limits of microbial cell detection, and our results show that the Atlantis Massif subsurface contains a relatively low density of microbial life compared to other subseafloor crustal and serpentinizing systems. This low density suggests that something may be limiting life in this subsurface habitat compared to the other habitats, such as energy availability, high pH, or low carbon dioxide availability, but further analyses are required to determine this.

## 4. Implications for understanding oceanic core complex processes

Expedition 357 was the first IODP expedition to successfully use seabed drills to acquire intact shallow mantle sequences at the top of the footwall of an oceanic detachment fault zone and to monitor borehole fluids while drilling. This expedition provides insights into magmatic, tectonic and alteration processes of an oceanic core complex that is actively undergoing serpentinization and has the potential to sustain a unique subsurface biosphere. The cores have exceptionally

well-preserved contacts and show strong lateral and vertical variations (from cm to m scale) in rock type and alteration assemblages that are a consequence of multiple phases of magmatism, fluid-rock interaction and mass transfer along the detachment fault zone. The results of this expedition are expected to address fundamental questions that were part of the motivation for the expedition (Früh-Green et al., 2015), such as: How are seafloor spreading and mantle melting linked to ocean crustal architecture? How do oceanic detachment faults develop and facilitate hydrothermal circulation? How do they affect the development of alteration patterns and the evolution of the deep biosphere in these environments?

IODP Expedition 357 sampled only the very shallowest level of the detachment fault zone and overlying talus blocks at the top of the massif. However, this is the first time that clear relationships of gabbro and dolerite hosted by mantle peridotite along the southern wall of Atlantis Massif have been documented. These relationships imply that melts are generated beneath volcanic-poor ridge segments at ridge-transform intersections, but much of the melt may be trapped in the mantle as it turns into lithosphere beneath the ridge axis, rather than migrating upward to form a continuous magmatic crust. Based on high-resolution ion microprobe (i.e., SHRIMP) U-Pb zircon ages from IODP Hole 1309D and broadly spaced samples collected along the southern ridge of Atlantis Massif, Grimes et al. (2008) document a protracted history of accretion in the footwall. They calculate a detachment fault slip rate of 28.7 ± 6.7 mm/a, which implies significant asymmetric plate spreading (up to 100% on the North American plate) for at least 200 ka during core complex formation. Our results are consistent with previous studies that indicate that ongoing magmatic activity associated with asymmetric plate spreading results in a heterogeneous mafic and ultramafic lithosphere with late dolerite intrusions exposed in the

638 denuded footwall, whereas accretion of volcanic seafloor persists in the hanging wall (Cannat et
639 al., 2006; Grimes et al., 2008; Ildefonse et al., 2007; John and Cheadle, 2010; Karson et al.,
640 2006; McCaig and Harris, 2012; Smith et al., 2006).
641
642 The volume of gabbros in the southern wall of the Atlantis Massif and their mode of intrusion as
643 thin lenses are distinct from the thick gabbroic sequence recovered at IODP Site U1309 (IODP
644 Expeditions 304 and 305) at the central dome (Blackman et al., 2006; Ildefonse et al., 2007;
645 McCaig et al., 2010; McCaig and Harris, 2012). Although a direct comparison of the two drilling
646 campaigns is difficult to make because of depth of penetration, and the possible tectonic control
647 on emplacement of rock sections, both campaigns yield important information about accretion
648 and alteration processes as well as regional heterogeneities associated with the architecture and
649 evolution of OCCs. The surface of the central dome was cored at IODP Hole U1309B, where
650 dike rocks and basalts were recovered, and a few pebbles of talc schist together with highly
651 altered basalt and dolerite were recovered in IODP Hole U1309H (Blackman et al., 2006; John et
652 al 2009). In addition, Alvin sampling during cruise AT3-60 in 2000 (MARVEL expedition;
653 Blackman et al., 2002) recovered one talc schist sample (sample 3642-1309; see Boschi et al.,
654 2008) along dive tracks in the vicinity of IODP Site U1309. Metasomatic talc-amphibole-chlorite
655 rocks are considered key components of detachment fault zones (e.g., Escartin et al., 2003;
656 Boschi et al., 2006a,b; McCaig et al., 2010) and pre-date dolerite diking events and basaltic
657 eruptions (Karson et al. 2006; McCaig and Harris, 2012). Although not abundant, the occurrence
658 of talc schists in the central dome of the Atlantis Massif hints at the presence of a thin
659 detachment fault zone in this area. However, on a regional scale, the newly acquired multibeam

660 data (Fig. 1) clearly allow the corrugated surface related to the detachment fault zone to be
661 distinguished.
662
663 The mineralogical assemblages, alteration textures, and bulk rock chemistries recorded in the
664 IODP Expedition 357 drill cores indicate progressive seawater infiltration along the detachment
665 fault and into the footwall, pointing to an important role of the mafic intrusions in controlling
666 fluid chemistry and metasomatism. Early high temperature, amphibolite-facies alteration and
667 ductile deformation features have been reported from studies of dredged and submersible
668 sampling of the southern wall (Boschi et al., 2006a; Karson et al., 2006; Schroeder and John,
669 2004), but such features are less common in the IODP Expedition 357 drill cores. In contrast,
670 alteration in the shallow IODP Expedition drill cores is dominated by serpentinization processes,
671 brittle deformation and mass transfer between mafic and ultramafic lithologies under
672 greenschist-facies conditions.
673
674 The occurrence of gabbroic intrusions is associated with talc-amphibole-chlorite metasomatism
675 and local blackwall formation and appears to increase from west to east. Metasomatism and talc
676 precipitation are most prevalent at contacts between mafic and ultramafic domains (Figs. 5 and
677 6.). A systematic overprinting of serpentinite by talc- and chlorite-rich assemblages is associated
678 with the occurrence of variably thick (micro)gabbroic lenses and points to silica mobility and
679 channelled fluid flow at varying depths within the detachment fault zone (see also Boschi et al.,
680 2006, 2008). The geochemical influence of the gabbroic intrusions and progressive fluid-rock
681 interaction is also evident from REE enrichments measured in serpentine minerals and tends to
682 increase from west to east (Rouméjon et al., 2018). The general trend to slightly larger volumes

683 of gabbroic intrusions from west to east (assuming the position of the drill holes roughly reflect
684 differing original depths in the lithosphere) suggests that magmatic activity may have been
685 greater at depth within the detachment fault zone before emplacement to their current locations.
686
687 The textural sequences and mineralogical assemblages in the ultramafic rocks reveal a transition
688 between an initial pervasive phase of hydration along grain boundaries to produce mesh-textures
689 in the serpentinites, with subsequent serpentinization and metasomatism focused along localized
690 fluid pathways (Rouméjon et al, 2018). Alteration commences as the peridotites and gabbros are
691 subjected to active hydrothermal circulation, but alteration of the dominant phase, olivine, to
692 produce serpentine minerals will be limited to temperatures below approximately 500°C
693 (Chernosky, 1973). Serpentinization of olivine becomes more effective below 350-400°C
694 (Evans, 2004) and reaches maximum rates between 250°-300°C (Andreani et al., 2007; Martin
695 and Fyfe, 1970; Malvoisin et al., 2012; McCollom 2016). Hydration is intense directly along the
696 detachment fault zone, where permeability is expected to be highest (McCaig et al., 2007;
697 McCaig et al., 2010), and progresses inside the footwall. When the fluids reach temperatures
698 below ~350°C, efficient serpentinization commences and is recorded by the development of
699 mesh texture at all sites. Based on zircon analyses and multicomponent magnetic remanence data
700 in the central dome, Schoolmeesters et al. (2012) proposed a model for the thermal structure of
701 the Atlantis Massif in which the 350°C isotherm corresponds to a depth of approximately 5 km
702 below the surface. Thus, initiation of serpentinization would have occurred at significant depths
703 and early in the exhumation history of the massif. The infiltration of seawater-derived
704 hydrothermal fluids is facilitated by the closely-spaced microfracture networks that crosscut the
705 olivine and result from combined thermal and tectonic stresses, enhanced by reaction-induced

706 permeability at the onset of serpentinization (Rouméjon and Cannat, 2014; Rouméjon et al.,
707 2018). As the footwall reaches shallower crustal levels, fluid flow will likely be dominated by
708 more continuous fracture planes that can channel hydrothermal fluids through the peridotite and
709 form veins (Andreani et al., 2007; Rouméjon et al., 2018). The transition from more pervasive
710 grain-boundary flow to localized or channeled flow is indicated by recrystallization of the mesh
711 texture to chrysotile-dominated serpentine and by banded veins (Rouméjon et al., 2018;
712 Rouméjon et al., this issue).
713
714 Talc formation postdates an early phase of serpentinization, and in some cases amphibole
715 formation (see also Boschi et al., 2006a), but predates late-stage intrusions and alteration of some
716 dolerite dikes and the extrusion of basalt, indicating that basaltic magmatism continued as the
717 variably altered basement sequences where emplaced on the seafloor. Alternating metasomatic
718 and serpentinized domains as well as irregular cross-cutting vein relationships in the IODP
719 Expedition 357 cores from the central (M0072 and M0076) and eastern sites (M0068) emphasize
720 the dynamic nature of the system with similar composition of veins forming at multiple times.
721 Textural relationships and the lateral and vertical distribution of metasomatic assemblages
722 indicate that Si ± Ca ± Al mass transfer occurred locally at peridotite/gabbro or
723 peridotite/dolorite contacts as well as through infiltration and interaction with Si-rich fluids along
724 fractures to form talc-rich assemblages (see also Boschi et al., 2006a; McCaig et al., 2010;
725 Rouméjon et al., 2018). In addition, the volume of carbonate veins was surprisingly low in the
726 recovered cores, even in the sites directly above the Lost City hydrothermal field. This suggests
727 that present-day fluid flow and hydrothermal activity at Lost City is localized by late normal
728 faults that cut the southern wall (Denny et al., 2015).

729

730 The presence of the mafic lenses within the serpentinites – and their alteration products to
731 mechanically weak minerals, such as talc, serpentine and chlorite – may also be critical to the
732 development of the detachment fault zone and may enhance unroofing of upper mantle
733 peridotites and lower crustal gabbroic rocks during seafloor spreading (Escartin et al., 2003;
734 Schroeder and John, 2004; Boschi et al., 2006b). Talc in particular may be influential in
735 lubricating and softening mylonitic shear zones and can lead to strain localization and focused
736 hydrothermal circulation along such faults (see also McCaig et al, 2010). In fact, low-T
737 detachment strain (< ~300°C) may actually be concentrated with time in the weak, talc-
738 serpentine-rich rocks, creating a runaway system and allowing movement on the detachment
739 fault zone to remain active while leaving a large portion of the exposed lithosphere undeformed.
740 In addition, based on detailed studies of greenschist- to amphibolite-facies assemblages in
741 metadolerites in the upper 130m of the IODP Site U1309D drill cores, McCaig and Harris (2012)
742 argue that the detachment fault zone itself acts as a conductive boundary layer between gabbroic
743 intrusions in the footwall and active hydrothermal circulation within the fault zone. They
744 conclude that widespread occurrences of gabbro at high levels in the crust below detachment
745 faults may be an expression of the same fundamental balance between magmatism and
746 hydrothermal circulation that produces a layered structure at fast-spreading ridges.
747

748 Although alteration in the IODP drill cores is dominated by earlier phases of serpentinization and
749 metasomatism associated with detachment faulting and denudation of mantle peridotites, wide-
750 scale, active serpentinization at Atlantis Massif is indicated by elevated concentrations of $H_2$ and
751 $CH_4$ in bottom water sampled before and after drilling. Even at the transform fault, $H_2$

concentrations in CTD casts were elevated (6.2 nM) relative to background seawater (<0.3 nM). Monitoring of the borehole fluids during drilling operations recorded numerous excursions in methane, temperature and ORP that often correlated with each other. The fact that the excursions occurred both while drilling as well as when no coring operations were taking place implies that horizons of reduced, and likely hydrogen-rich, fluids must exist in the basement rocks and that volatiles are being continuously expelled during active serpentinization at the Atlantis Massif. Active volatile expulsion was also indicated as bubbles emitting from Site M0070. The diffuse fluid flow indicated by the sensor package data and water sampling during IODP Expedition 357 contrasts strongly with the focused flow associated with the actively venting Lost City hydrothermal field. The detachment fault zone seems to play a passive role in channelling the basement fluids. Instead, present-day hydrothermal fluid flow is likely controlled by late-stage normal faults cutting the southern wall (Fig. 1; see also Denny et al., 2015). In addition, the present-day hydrothermal fluids, characterized by high pH, low Si, and low metal concentrations are controlled by serpentinization reactions and are chemically distinct from the higher temperature fluids that were involved with mass transfer and metasomatism at deeper levels of the detachment fault zone and at earlier stages in the evolution of the Atlantis Massif.

A major achievement of IODP Expedition 357 was to obtain microbiological samples along the west-east lithospheric age profile, which will provide a better understanding of how microbial communities evolve as ultramafic rocks are emplaced on the seafloor. Our results indicate that the subsurface of the serpentinite basement of Atlantis Massif has relatively low biomass. We anticipate that on-going post-cruise microbiological studies will provide important constraints to address basic questions, such as what is the nature of microbial communities hosted by

serpentinizing rocks, and to what depth is microbial activity sustained? How do these vary with aging of the lithosphere? How do they differ from or interact with communities in sediments and mafic substrates in the same age crust? Because of the significant difference in volatile compositions and limited $CO_2$ stability at high pH, one can expect that biotopes hosted in serpentinizing environments will differ significantly from axial, basaltic-hosted vent systems in which $CO_2$ is a dominant volatile species. In addition, the mixing of oxidized seawater with highly reduced fluids leads to complex gradients in fluid chemistry and possibly temperature that may influence microbial distribution and activity. Substantially different habitats harboring various types of aerobic and anaerobic metabolisms may thus occur over a narrow spatial scale in these types of environments.

**Acknowledgements**

We thank the captain and crew aboard the RRS James Cook and the ESO staff for their efforts and support during all phases of IODP Expedition 357. Funding by ECORD is gratefully acknowledged and each of the IODP Exp. 357 participants thanks their representative national funding agencies for IODP support to participate in the expedition and conduct post-cruise studies. This contribution was greatly improved by the thoughtful and thorough reviews from an anonymous reviewer and Nicholas Haymon.

**Supplementary Material**

Appendix A. Synthesis of the lithological contacts, mineralogies and off shore analyses of the western Hole M0071A (IODP Expedition 357).

Appendix B. Synthesis of the lithological contacts, mineralogies and off shore analyses of the western Hole M0071B (IODP Expedition 357).

Appendix C. Synthesis of the lithological contacts, mineralogies and off shore analyses of the western Hole M0071C (IODP Expedition 357).

Appendix D. Synthesis of the lithological contacts, mineralogies and off shore analyses of the central Hole M0069A (IODP Expedition 357).

Appendix E. Synthesis of the lithological contacts, mineralogies and off shore analyses of the central Hole M0072B, IODP Expedition 357 (Part 1).

Appendix F. Synthesis of the lithological contacts, mineralogies and off shore analyses of the central Hole M0072B, IODP Expedition 357 (Part 2).

Appendix G. Synthesis of the lithological contacts, mineralogies and off shore analyses of the central Hole M0076B, IODP Expedition 357 (Part 1).

Appendix H. Synthesis of the lithological contacts, mineralogies and off shore analyses of the central Hole M0076B, IODP Expedition 357 (Part 2).

Appendix I. Synthesis of the lithological contacts, mineralogies and off shore analyses of eastern Hole M0068B (IODP Expedition 357).

Appendix J. Synthesis of the lithological contacts, mineralogies and off shore analyses of eastern Hole M0075B (IODP Expedition 357).

**References**

Alt, J.C., Shanks, W.C., III, 2003. Serpentinization of abyssal peridotites from the MARK area, Mid-Atlantic Ridge: sulfur geochemistry and reaction modeling. Geochimica et Cosmochimica Acta 67(4), 641–653.

Andreani, M., Mével, C., Boullier, A.-M., Escartin, J., 2007. Dynamic control on serpentine crystallization in veins: constraints on hydration processes in oceanic peridotites. Geochemistry, Geophysics, Geosystems 8(2), Q02012.

Blackman, D.K., Karson, J.A., Kelley, D.S., Cann, J.R., Früh-Green, G.L., Gee, J.S., Hurst, S.D., John, B.E. Morgan, J., Nooner, S.L., Ross, D.K., Schroeder, T.J., Williams, E.A., 2002. Geology of the Atlantis Massif (Mid-Atlantic Ridge, 30°N): implications for the evolution of an ultramafic oceanic core complex. Marine Geophysical Research 23(5–6), 443–469.

Blackman, D.K., Ildefonse, B., John, B.E., Ohara, Y., Miller, D.J., MacLeod, C.J., the Expedition 304/305 Scientists, 2016. Proceedings of the Integrated Ocean Drilling Program, Volume 304/305: College Station, TX, Integrated Ocean Drilling Program Management International, Inc., doi: 10.2204/iodp. proc.304305.2006.

842 Boschi, C., Früh-Green, G.L., Delacour, A., Karson, J.A., Kelley, D.S., 2006a. Mass transfer and
843 fluid flow during detachment faulting and development of an oceanic core complex, Atlantis
844 Massif (MAR 30°N). Geochemistry, Geophysics, Geosystems 7(1), Q01004.
845 Boschi, C., Früh-Green, G.L., Escartin, J., 2006b. Occurrence and significance of serpentinite-
846 hosted, talc-rich fault rocks in modern oceanic settings and ophiolite complexes. Ofioliti 31(2),
847 123-134.
848 Boschi, C., Dini, A., Früh-Green, G.L., Kelley, D.S., 2008. Isotopic and element exchange during
849 serpentinization and metasomatism at the Atlantis Massif (MAR 30°N): insights from B and Sr
850 isotopes. Geochimica et Cosmochimica Acta 72(7), 1801–1823.
851 Brazelton, W.J., Baross, J.A., 2009. Abundant transposases encoded by the metagenome of a
852 hydrothermal chimney biofilm. ISME Journal 3(12), 1420–1424.
853 Brazelton, W.J., Schrenk, M.O., Kelley, D.S., Baross, J.A., 2006. Methane- and sulfur-
854 metabolizing microbial communities dominate the Lost City hydrothermal field ecosystem.
855 Applied and Environmental Microbiology 72(9), 6257–6270.
856 Brazelton, W.J., Thornton, C.N., Hyer, A, Twing, K.I., Longino, A.A., Lang, S.Q., Lilley, M.D.,
857 Früh-Green, G.L., Schrenk, M.O., 2017. Metagenomic identification of active methanogens and
858 methanotrophs in serpentinite springs of the Voltri Massif, Italy. PeerJ 5:e2945
859 https://doi.org/10.7717/peerj.2945.
860 Cann, J.R., Blackman, D.K., Smith, D.K., McAllister, E., Janssen, B., Mello, S., Avgerinos, E.,
861 Pascoe, A.R., Escartín, J., 1997, Corrugated slip surfaces formed at ridge-transform
862 intersections on the Mid-Atlantic Ridge Nature 385, 329–332.
863 Cannat, M., 1993. Emplacement of mantle rocks in the seafloor at mid-ocean ridges. Journal of
864 Geophysical Research: Solid Earth 98(B3), 4163–4172.

865 Cannat, M., Sauter, D., Mendel, V., Ruellan, E., Okino, K., Escartin, J., Combier, V., and Baala,
866 M., 2006. Modes of seafloor generation at a melt-poor ultraslow-spreading ridge. Geology
867 34(7), 605–608.
868 Chernosky, J. V. J., 1973. An experimental investigation of the serpentine and chlorite group
869 minerals in the system MgO-Al2O3 – SiO2 – H2O, Ph.D. thesis, Mass. Inst. of Tech- nol.,
870 Cambridge.
871 Delacour, A., Früh-Green, G.L., Bernasconi, S.M., Schaeffer, P., Kelley, D.S., 2008. Carbon
872 geochemistry of serpentinites in the Lost City hydrothermal system (30°N, MAR). Geochimica
873 et Cosmochimica Acta 72(15), 3681–3702.
874 Denny, A.R., Kelley, D.S., and Früh-Green, G.L., 2015. Geologic Evolution of the Lost City
875 Hydrothermal Field: Geochemistry, Geophysics, Geosystems 17, 375–394, doi:10.1002/
876 2015GC005869.
877 Dick, H.J.B., Tivey, M.A., Tucholke, B.E., 2008. Plutonic foundation of a slow-spreading ridge
878 segment: oceanic core complex at Kane Megamullion, 23°30′N, 45°20′W. Geochemistry,
879 Geophysics, Geosystems 9(5), Q05014.
880 Escartín, J., Canales, J. P., 2011. Detachments in oceanic lithosphere: Deformation, magmatism,
881 fluid flow, and ecosystems. Eos, Transactions American Geophysical Union 92(4), 31-31.
882 Escartín, J., Mével, C., MacLeod, C.J., and McCaig, A.M., 2003. Constraints on deformation
883 conditions and the origin of oceanic detachments: the Mid- Atlantic Ridge core complex at 15
884 ° 45′ N. Geochemistry, Geophysics, Geo- systems, 4(8):1067.
885 http://dx.doi.org/10.1029/2002GC000472.

886 Escartín, J., Andreani, M., Hirth, G., Evans, B., 2008. Relationships between the microstructural
887 evolution and the rheology of talc at elevated pressures and temperatures. Earth and Planetary
888 Science Letters 268(3–4), 463–475.

889 Evans, B. W., 2004. The Serpentinite Multisystem Revisited: Chrysotile Is Metastable.
890 International Geology Review, 46(6), 479–506. http://doi.org/10.2747/0020-6814.46.6.479

891 Früh-Green, G.L., Kelley, D.S., Bernasconi, S.M., Karson, J.A., Ludwig, K.A., Butterfield, D.A.,
892 Boschi, C., Proskurowksi, G., 2003. 30,000 years of hydrothermal activity at the Lost City vent
893 field. Science 301(5632), 495–498.

894 Früh-Green, G.L., Connolly, J.A.D., Plas, A., Kelley, D.S., Grobéty, B., 2004. Serpentinization of
895 oceanic peridotites: implications for geochemical cycles and biological activity. In Wilcock,
896 W.S.D., DeLong, E.F., Kelley, D.S., Baross, J.A., Cary, C., The Subseafloor Biosphere at Mid-
897 Ocean Ridges. Geophysical Monograph 144, 119–136.

898 Früh-Green, G.L., Orcutt, B.N., and Green, S., 2015. Expedition 357 Scientific Prospectus: Atlantis
899 Massif Serpentinization and Life. International Ocean Discovery Program.
900 http://dx.doi.org/10.14379/iodp.sp.357.2015.

901 Früh-Green, G.L., Orcutt, B.N., Green, S., Cotterill, C., and the Expedition 357 Scientists,
902 2016. Expedition 357 Preliminary Report: Atlantis Massif Serpentinization and
903 Life. International Ocean Discovery Program. http://dx.doi.org/10.14379/iodp.pr.357.2016

904 Früh-Green, G.L., Orcutt, B.N., Green, S.L., Cotterill, C., Morgan, S., Akizawa, N., Bayrakci,
905 G., Behrmann, J.-H., Boschi, C., Brazelton, W.J., Cannat, M., Dunkel, K.G., Escartin, J.,
906 Harris, M., Herrero-Bervera, E., Hesse, K., John, B.E., Lang, S.Q., Lilley, M.D., Liu, H.-Q.,
907 Mayhew, L.E., McCaig, A.M., Menez, B., Morono, Y., Quéméneur, M., Rouméjon, S.,
908 Sandaruwan Ratnayake, A., Schrenk, M.O., Schwarzenbach, E.M., Twing, K.I., Weis, D.,

Whattam, S.A., Williams, M., Zhao, R., 2017a. Expedition 357 summary, in Früh-Green, G.L., Orcutt, B.N., Green, S.L., Cotterill, C., and the Expedition 357 Scientists, Atlantis Massif Serpentinization and Life. Proceedings of the International Ocean Discovery Program, 357: College Station, TX. http://dx.doi.org/10.14379/iodp.proc.357.101.2017.

Früh-Green, G.L., Orcutt, B.N., Green, S.L., Cotterill, C., Morgan, S., Akizawa, N., Bayrakci, G., Behrmann, J.-H., Boschi, C., Brazelton, W.J., Cannat, M., Dunkel, K.G., Escartin, J., Harris, M., Herrero-Bervera, E., Hesse, K., John, B.E., Lang, S.Q., Lilley, M.D., Liu, H.-Q., Mayhew, L.E., McCaig, A.M., Menez, B., Morono, Y., Quéméneur, M., Rouméjon, S., Sandaruwan Ratnayake, A., Schrenk, M.O., Schwarzenbach, E.M., Twing, K.I., Weis, D., Whattam, S.A., Williams, M., Zhao, R., 2017b. Expedition 357 methods, in Früh-Green, G.L., Orcutt, B.N., Green, S.L., Cotterill, C., and the Expedition 357 Scientists, Atlantis Massif Serpentinization and Life. Proceedings of the International Ocean Discovery Program, 357: College Station, TX. http://dx.doi.org/10.14379/iodp.proc.357.102.2017.

Früh-Green, G.L., Orcutt, B.N., Green, S.L., Cotterill, C., Morgan, S., Akizawa, N., Bayrakci, G., Behrmann, J.-H., Boschi, C., Brazelton, W.J., Cannat, M., Dunkel, K.G., Escartin, J., Harris, M., Herrero-Bervera, E., Hesse, K., John, B.E., Lang, S.Q., Lilley, M.D., Liu, H.-Q., Mayhew, L.E., McCaig, A.M., Menez, B., Morono, Y., Quéméneur, M., Rouméjon, S., Sandaruwan Ratnayake, A., Schrenk, M.O., Schwarzenbach, E.M., Twing, K.I., Weis, D., Whattam, S.A., Williams, M., Zhao, R., 2017c. Eastern sites, in Früh-Green, G.L., Orcutt, B.N., Green, S.L., Cotterill, C., and the Expedition 357 Scientists, Atlantis Massif Serpentinization and Life. Proceedings of the International Ocean Discovery Program, 357: College Station, TX. http://dx.doi.org/10.14379/iodp.proc.357.103.2017.

Früh-Green, G.L., Orcutt, B.N., Green, S.L., Cotterill, C., Morgan, S., Akizawa, N., Bayrakci, G., Behrmann, J.-H., Boschi, C., Brazelton, W.J., Cannat, M., Dunkel, K.G., Escartin, J., Harris, M., Herrero-Bervera, E., Hesse, K., John, B.E., Lang, S.Q., Lilley, M.D., Liu, H.-Q., Mayhew, L.E., McCaig, A.M., Menez, B., Morono, Y., Quéméneur, M., Rouméjon, S., Sandaruwan Ratnayake, A., Schrenk, M.O., Schwarzenbach, E.M., Twing, K.I., Weis, D., Whattam, S.A., Williams, M., Zhao, R., 2017d. Central sites, in Früh-Green, G.L., Orcutt, B.N., Green, S.L., Cotterill, C., and the Expedition 357 Scientists, Atlantis Massif Serpentinization and Life. Proceedings of the International Ocean Discovery Program, 357: College Station, TX. http://dx.doi.org/10.14379/iodp.proc.357.104.2017.

Früh-Green, G.L., Orcutt, B.N., Green, S.L., Cotterill, C., Morgan, S., Akizawa, N., Bayrakci, G., Behrmann, J.-H., Boschi, C., Brazelton, W.J., Cannat, M., Dunkel, K.G., Escartin, J., Harris, M., Herrero-Bervera, E., Hesse, K., John, B.E., Lang, S.Q., Lilley, M.D., Liu, H.-Q., Mayhew, L.E., McCaig, A.M., Menez, B., Morono, Y., Quéméneur, M., Rouméjon, S., Sandaruwan Ratnayake, A., Schrenk, M.O., Schwarzenbach, E.M., Twing, K.I., Weis, D., Whattam, S.A., Williams, M., Zhao, R., 2017e. Western sites, in Früh-Green, G.L., Orcutt, B.N., Green, S.L., Cotterill, C., and the Expedition 357 Scientists, Atlantis Massif Serpentinization and Life. Proceedings of the International Ocean Discovery Program, 357: College Station, TX. http://dx.doi.org/10.14379/iodp.proc.357.102.2017.

Früh-Green, G.L., Orcutt, B.N., Green, S.L., Cotterill, C., Morgan, S., Akizawa, N., Bayrakci, G., Behrmann, J.-H., Boschi, C., Brazelton, W.J., Cannat, M., Dunkel, K.G., Escartin, J., Harris, M., Herrero-Bervera, E., Hesse, K., John, B.E., Lang, S.Q., Lilley, M.D., Liu, H.-Q., Mayhew, L.E., McCaig, A.M., Menez, B., Morono, Y., Quéméneur, M., Rouméjon, S., Sandaruwan Ratnayake, A., Schrenk, M.O., Schwarzenbach, E.M., Twing, K.I., Weis, D.,

954 Whattam, S.A., Williams, M., Zhao, R., 2017f. Northern sites, in Früh-Green, G.L., Orcutt,
955 B.N., Green, S.L., Cotterill, C., and the Expedition 357 Scientists, Atlantis Massif
956 Serpentinization and Life. Proceedings of the International Ocean Discovery Program, 357:
957 College Station, TX.Northern sites. http://dx.doi.org/10.14379/iodp.proc.357.106.2017.
958 Grimes, C.B., John, B.E., Cheadle, M.J., Wooden, J.L., 2008. Protracted construction of
959 gabbroic crust at a slow spreading ridge: constraints from $^{206}Pb/^{238}U$ zircon ages from Atlantis
960 Massif and IODP Hole U1309D (30°N, MAR). Geochemistry, Geophysics, Geosystems, 9,
961 Q08012.
962 Holm, N.G., Charlou, J.L., 2001. Initial indications of abiotic formation of hydrocarbons in the
963 Rainbow ultramafic hydrothermal system, Mid-Atlantic Ridge. Earth and Planetary Science
964 Letters, 191(1–2), 1–8.
965 Ildefonse, B., Blackman, D.K., John, B.E., Ohara, Y., Miller, D.J., MacLeod, C.J., Integrated
966 Ocean Drilling Program Expeditions 304/305 Science Party, 2007. Oceanic core complexes and
967 crustal accretion at slow-spreading ridges. Geology 35(7), 623–626.
968 Jagoutz, E., Palme, H., Baddenhausen, H., Blum, K., Cendales, M., Dreibus, G., Spettel, B.,
969 Lorenz, V., Vanke, H., 1979. The abundance of major, minor and trace elements in the earth's
970 mantle as derived from primitive ultramafic nodules. Geochimica et Cosmochimica Acta 11
971 (2), 2031–2050.
972 John, B. E., Cheadle, M. J., 2010. Deformation and alteration associated with oceanic and
973 continental detachment fault systems; are they similar? Geophysical Monograph 188, 175-
974 205.
975 John, B.E., Cheadle, M.J., Gee, J.S., Grimes, C.B., Morris, A., and Pressling, N., 2009. Data
976 report: spatial and temporal evolution of slow spread oceanic crust—graphic sections of core

977 recovered from IODP Hole U1309D, Atlantis Massif, 30°N, MAR (including Pb/U zircon
978 geochronology and magnetic remanence data). In Blackman, D.K., Ildefonse, B., John, B.E.,
979 Ohara, Y., Miller, D.J., MacLeod, C.J., and the Expedition 304/305 Scientists, Proc.
980 IODP, 304/305: College Station, TX (Integrated Ocean Drilling Program Management
981 International, Inc.). doi:10.2204/iodp.proc.304305.205.2009.
982 Jørgensen, S.L., Zhao, R , 2016. Microbial Inventory of Deeply Buried Oceanic Crust from a
983 Young Ridge Flank. Frontiers in Microbiology 7:820. doi: 10.3389/fmicb.2016.00820.
984 Karson, J.A., Früh-Green, G.L., Kelley, D.S., Williams, E.A., Yoerger, D.R., Jakuba, M., 2006.
985 Detachment shear zone of the Atlantis Massif core complex, Mid-Atlantic Ridge, 30°N.
986 Geochemistry, Geophysics, Geosystems 7(6), Q06016.
987 Kelemen, P. B., Dick, H. J., Quick, J. E., 1992. Formation of harzburgite by pervasive melt/rock
988 reaction in the upper mantle. Nature 358(6388), 635-641.
989 Kelemen, P.B., Kikawa, E., Miller, D.J., Shipboard Scientific Party, 2007. Leg 209 summary:
990 processes in a 20-km-thick conductive boundary layer beneath the Mid-Atlantic Ridge, 14°–
991 16°N. In Kelemen, P.B., Kikawa, E., Miller, D.J. (Eds.), Proceedings of the Ocean Drilling
992 Program, Scientific Results, 209: College Station, TX (Ocean Drilling Program), 1–33.
993 Kelley, D.S., Karson, J.A., Blackman, D.K., Früh-Green, G.L., Butterfield, D.A., Lilley, M.D.,
994 Olson, E.J., Schrenk, M.O., Roe, K.K., Lebon, G.T., Rivizzigno, P., the AT3-60 Shipboard
995 Party, 2001. An off-axis hydrothermal vent field near the Mid-Atlantic Ridge at 30°N. Nature
996 412(6843), 145–149.
997 Kelley, D.S., Karson, J.A., Früh-Green, G.L., Yoerger, D.R., Shank, T.M., Butterfield, D.A.,
998 Hayes, J.M., Schrenk, M.O., Olson, E.J., Proskurowski, G., Jakuba, M., Bradley, A., Larson, B.,
999 Ludwig, K., Glickson, D., Buckman, K., Bradley, A.S., Brazelton, W.J., Roe, K., Elend, M.J.,

1000 Delacour, A., Bernasconi, S.M., Lilley, M.D., Baross, J.A., Summons, R.E., Sylva, S.P., 2005.
1001 A serpentinite-hosted ecosystem: the Lost City hydrothermal field. Science 307(5714), 1428–
1002 1434.
1003 Konn, C., Charlou, J.L., Donval, J.P., Holm, N.G., Dehairs, F., Bouillon, S., 2009. Hydrocarbons
1004 and oxidized organic compounds in hydrothermal fluids from Rainbow and Lost City
1005 ultramafic-hosted vents. Chemical Geology 258(3–4), 299–314.
1006 Lang, S.Q., Butterfield, D.A., Schulte, M., Kelley, D.S., Lilley, M.D., 2010. Elevated
1007 concentrations of formate, acetate and dissolved organic carbon found at the Lost City
1008 hydrothermal field. Geochimica et Cosmochimica Acta 74(3), 941–952.
1009 Lang, S.Q., Früh-Green, G.L., Bernasconi, S.M., Lilley, M.D., Proskurowski, G., Méhay, S.,
1010 Butterfield, D.A., 2012. Microbial utilization of abiogenic carbon and hydrogen in a
1011 serpentinite-hosted system. Geochimica et Cosmochimica Acta 92, 82–99.
1012 Lang S.Q., Früh-Green G.L., Bernasconi S.M., Brazelton W.J., Schrenk, M.O., and McGonigle, J.,
1013 2018. Deeply-sourced formate fuels sulfate reducers but not methanogens at Lost City
1014 hydrothermal field. Nature Scientific Reports 8, 755.
1015 Ludwig, K.A., Kelley, D.S., Butterfield, D.A., Nelson, B.K., Früh-Green, G.L., 2006. Formation
1016 and evolution of carbonate chimneys at the Lost City hydrothermal field. Geochimica et
1017 Cosmochimica Acta 70(14), 3625–3645.
1018 Martin, B. and Fyfe, W.S., 1970. Some experimental and theoretical observations on the kinetics of
1019 hydration reactions with par-ticular reference to serpentinization, Chemical Geology 6, 185-195.
1020 Mason, .U., Nakagawa, T., Rosner, M., Van Nostrand, J.D., Zhou, J., Maruyama, A., Fisk, M.R.,
1021 Giovannoni, S.J., 2010. First investigation of the microbiology of the deepest layer of ocean
1022 crust. PLoS One 5(11), e15399.

1023 Malvoisin, B., Brunet, F., Carlut, J., Rouméjon, S. & Cannat, M., 2012. Serpentinization of oceanic
1024 peridotites: 2. Kinetics and processes of San Carlos olivine hydrothermal alteration. Journal of
1025 Geophysical Research 117, B04102, doi:10.1029/2011JB008842.
1026 McCaig, A.M., Delacour, A., Fallick, A.E., Castelain, T., Früh-Green G.L., 2010. Fluid
1027 circulation and isotopic alteration in and beneath oceanic detachment faults in the Central
1028 Atlantic: Implications for the geometry and evolution of high-temperature hydrothermal
1029 circulation cells at slow-spreading ridges, In: Diversity of Hydrothermal Systems on Slow
1030 Spreading Ocean Ridges, eds PA Rona, CW Devey, J Dyment, BJ Murton, AGU Geophy.
1031 Mono. Series 188:207-239.
1032 McCaig, A.M., Harris, M., 2012. Hydrothermal circulation and the dike-gabbro transition in the
1033 detachment mode of slow seafloor spreading. Geology 40, 367-370. doi: 10.1130/G32789.1.
1034 McCollom, T.M., 2016. Abiotic methane formation during serpentinization. Proceedings of the
1035 National Academy of Sciences 113 (49) 13965-13970; DOI:10.1073/pnas.1611843113.
1036 Méhay, S., Früh-Green, G.L., Lang, S.Q., Bernasconi, S.M., Brazelton, W.J., Schrenk, M.O.,
1037 Schaeffer, P., Adam, P., 2013. Record of archaeal activity at the serpentinite-hosted Lost City
1038 hydrothermal field. Geobiology 11(6), 570–592.
1039 Morono, Y., Inagaki, F., Heuer, V.B., Kubo, Y., Maeda, L., Bowden, S., Cramm, M., Henkel, S.,
1040 Hirose, T., Homola, K., Hoshino, T., Ijiri, A., Imachi, H., Kamiya, N., Kaneko, M., Lagostina,
1041 L., Manners, H., McClelland, H.-L., Metcalfe, K., Okutsu, N., Pan, D., Raudsepp, M.J.,
1042 Sauvage, J., Schubotz, F., Spivack, A., Tonai, S., Treude, T., Tsang, M.-Y., Viehweger, B.,
1043 Wang, D.T., Whitaker, E., Yamamoto, Y., and Yang, K., 2017. Expedition 370 methods. In
1044 Heuer, V.B., Inagaki, F., Morono, Y., Kubo, Y., Maeda, L., and the Expedition 370 Scientists,
1045 Temperature Limit of the Deep Biosphere off Muroto. Proceedings of the International Ocean

Discovery Program, 370: College Station, TX (International Ocean Discovery Program). https://doi.org/10.14379/iodp.proc.370.102.2017

Nicolas, A., 1986. Structure and petrology of peridotites: Clues to their geodynamic environment. Reviews of Geophysics 24 (4), 875-895.

Nicolas, A., Prinzhofer, A. (1983) Cumulative or residual origin for the transition zone in ophiolites: structural evidence. Journal of Petrology 24, 188–206.

Niu, Y., 2004. Bulk-rock major and trace element compositions of abyssal peridotites: implications for mantle melting, melt extraction and post-melting processes beneath mid-ocean ridges. Journal of Petrology 45, 2423–2458.

Orcutt, B.N., Bergenthal, M., Freudenthal, T., Smith, D., Lilley, M.D., Schnieders, L., Green, S., Früh-Green, G.L., 2017. Contamination tracer testing with seabed drills: IODP Expedition 357. Scientific Drilling 23, 39–46.

Paulick, H., Bach,W., Godard, M., De Hoog, J.C.M., Suhr, G., Harvey, J., 2006. Geochemistry of abyssal peridotites (Mid-Atlantic Ridge, 15°20′N, ODP Leg 209): implications for fluid/rock interaction in slow spreading environments. Chemical Geology 234, 179–210.

Proskurowski, G., Lilley, M.D., Kelley, D.S., Olson, E.J., 2006. Low temperature volatile production at the Lost City hydrothermal field, evidence from a hydrogen stable isotope geothermometer. Chemical Geology 229(4), 331–343.

Proskurowski, G., Lilley, M.D., Seewald, J.S., Früh-Green, G.L., Olson, E.J., Lupton, J.E., Sylva, S.P., Kelley, D.S., 2008. Abiogenic hydrocarbon production at Lost City hydrothermal field. Science 319(5863), 604–607.

1067 Rouméjon, S., Cannat, M., 2014. Serpentinization of mantle-derived peridotites at mid-ocean
1068 ridges: Mesh texture development in the context of tectonic exhumation. Geochemistry,
1069 Geophysics, Geosystems 15, 2354–2379.
1070 Rouméjon, S., Cannat, M., Agrinier, P., Godard, M. & Andreani, M., 2015. Serpentinization and
1071 Fluid Pathways in Tectonically Exhumed Peridotites from the Southwest Indian Ridge (62-65
1072 E). Journal of Petrology 56, 703–734.
1073 Rouméjon, S., Früh-Green, G.L., Orcutt, B.N., and the IODP Expedition 357 Science Party,
1074 2018. Alteration heterogeneities in peridotites exhumed on the southern wall of the Atlantis
1075 Massif (IODP Expedition 357). Journal of Petrology, 2018, 1-29, doi:
1076 10.1093/petrology/egy065.
1077 Rouméjon, S., Williams, M.J., Früh-Green, G.L., this issue. In situ oxygen isotope analyses in
1078 serpentine minerals: constraints on serpentinization during tectonic exhumation at slow- and
1079 ultraslow-spreading ridges.
1080 Schoolmeesters, N., M. J. Cheadle, B. E. John, P. W. Reiners, J. Gee, and C. B. Grimes (2012),
1081 The cooling history and the depth of detachment faulting at the Atlantis Massif oceanic core
1082 complex, Geochemistry, Geophysics, Geosystems 13, Q0AG12, doi:10.1029/2012GC004314.
1083 Schrenk, M.O., Kelley, D.S., Bolton, S.A., Baross, J.A., 2004. Low archaeal diversity linked to
1084 subseafloor geochemical processes at the Lost City hydrothermal field, Mid-Atlantic Ridge.
1085 Environmental Microbiology 6, 1086–1095.
1086 Schrenk, M.O., Brazelton, W.J., Lang, S.Q., 2013. Serpentinization, carbon, and deep life.
1087 Reviews in Mineralogy and Geochemistry 75 (1), 575-606.
1088 Schroeder, T., John, B., Frost, B.R., 2002. Geologic implications of seawater circulation through
1089 peridotite exposed at slow-spreading mid-ocean ridges. Geology 30(4), 367–370.

1090 Schroeder, T., John, B.E., 2004. Strain localization on an oceanic detachment fault system,
1091 Atlantis Massif, 30°N, Mid-Atlantic Ridge. Geochemistry, Geophysics, Geosystems 5,
1092 Q11007.
1093 Schwarzenbach E.M., Früh-Green G.L., Bernasconi S.M., Alt J.C, Shanks III W.C., Gaggero
1094 Laura Crispini, L. 2012. Sulfur geochemistry of peridotite-hosted hydrothermal systems:
1095 Comparing the Ligurian ophiolites with oceanic serpentinites. Geochimica Cosmochimica
1096 Acta 91, 283–305.
1097 Smith, D.K., Cann, J.R., Escartin, J., 2006. Widespread active detachment faulting and core
1098 complex formation near 13°N on the Mid-Atlantic Ridge. Nature 442(7101), 440–443.
1099 Smith, D.K., Escartín, J., Schouten, H., Cann, J.R., 2008. Fault rotation and core complex
1100 formation: significant processes in seafloor formation at slow-spreading mid-ocean ridges (Mid-
1101 Atlantic Ridge, 13°–15°N). Geochemistry, Geophysics, Geosystems 9(3), Q03003.
1102 Tucholke, B.E., Behn, M.D., Buck, W.R., Lin, J., 2008. Role of melt supply in oceanic detachment
1103 faulting and formation of megamullions. Geology 36(6), 455–458.
1104
1105

Table 1. IODP Expedition 357 site locations, core recovery, and maximum volatile concentrations.

| Hole | Latitude | Longitude | Water depth (m) | Drill | Number of cores | Interval cored (m) | Core recovered (m) | Core recovery (%) | Interval open-holed (m) | Penetration depth (mbsf) | Maximum hydrogen (nM)* | Maximum methane (nM)* |
|---|---|---|---|---|---|---|---|---|---|---|---|---|
| Eastern Sites | | | | | | | | | | | | |
| M0068A | 30°7.49'N | 42°5.74'W | 1102.7 | RD2 | 1 | 1.97 | 0.47 | 23.9 | 0 | 1.97 | 34 | BDL |
| M0068B | 30°7.51'N | 42°5.75'W | 1102 | RD2 | 9 | 9.6 | 6.34 | 66.04 | 0 | 9.6 | 137 | BDL |
| M0075A | 30°7.67'N | 42°3.98'W | 1568 | RD2 | 1 | 1.72 | 0.65 | 37.79 | 0 | 1.72 | 3 | BDL |
| M0075B | 30°7.65'N | 42°3.97'W | 1568 | RD2 | 3 | 5.7 | 2.73 | 47.88 | 0 | 5.7 | | BDL |
| Central Sites | | | | | | | | | | | | |
| M0069A | 30°7.94'N | 42°7.20'W | 850.9 | RD2 | 10 | 16.44 | 12.29 | 75 | 0 | 16.44 | 58 | 4 |
| M0072A | 30°7.79'N | 42°7.32'W | 820.3 | RD2 | 2 | 2.23 | 0.87 | 39.1 | 0 | 2.23 | 12 | 2 |
| M0072B | 30°7.79'N | 42°7.32'W | 820.3 | RD2 | 8 | 11.61 | 6.49 | 52.3 | 0.825 | 12.43 | 323 | 2 |
| M0076A | 30°7.62'N | 42°7.08'W | 768 | RD2 | 1 | 1.72 | 0.4 | 23.26 | 0 | 1.72 | – | – |
| M0076B | 30°7.62'N | 42°7.07'W | 768 | RD2 | 10 | 16.31 | 11.71 | 71.8 | 0 | 16.31 | 12 | 3 |
| Western Sites | | | | | | | | | | | | |
| M0071A | 30°7.71'N | 42°9.20'W | 1390.8 | MeBo | 2 | 5.22 | 2.85 | 54.6 | 0 | 5.22 | 61 | BDL |
| M0071B | 30°7.72'N | 42°9.19'W | 1380 | RD2 | 3 | 4.3 | 2.31 | 53.62 | 0 | 4.3 | 8 | BDL |
| M0071C | 30°7.70'N | 42°9.21'W | 1390 | MeBo | 9 | 12.15 | 4.44 | 30.29 | 0 | 12.15 | 6 | BDL |
| M0073A | 30°7.90'N | 42°10.97'W | 1430.2 | MeBo | 1 | 2.2 | 0 | 0 | 0 | 2.2 | 40 | BDL |
| Northern Sites | | | | | | | | | | | | |
| M0070A | 30°8.55'N | 42°8.19'W | 1140.5 | MeBo | 3 | 4 | 2.09 | 52.25 | 0 | 4 | 73 | 2 |
| M0070B | 30°8.54'N | 42°8.16'W | 1140.5 | RD2 | 1 | 1.3 | 0.38 | 29.23 | 0 | 1.3 | 5 | 5 |
| M0070C | 30°8.54'N | 42°8.19'W | 1140.5 | MeBo | 3 | 5.21 | 2.21 | 42.42 | 0 | 5.21 | – | – |
| M0074A | 30°9.87'N | 42°7.32'W | 1550 | MeBo | 1 | 2.68 | 0.86 | 32.09 | 0 | 2.68 | BDL | BDL |

Notes: * Maximum dissolved concentrations in waters sampled after drilling. Full data set of hydrogen and methane concentrations in Früh-Green et al., 2017c.
http://publications.iodp.org/proceedings/357/EXP_REPT/TABLES/357_103/357_103_T12.CSV
BDL = Below detection limited

Table 2. Bulk rock chemical compositions of representative lithologies from IODP Exp. 357

| Hole | M0071A | M0071A | M0071C | M0071C | M0069A | M0069A | M0069A | M0069A | M0072B | M0072B | M0072B | M0072B | M0076B | M0068A | M0068B | M0068B | M0068B | M0068B | M0075B |
|---|---|---|---|---|---|---|---|---|---|---|---|---|---|---|---|---|---|---|---|
| Core | 1R-2 | 2R-1 | 1R-1 | 2R-1 | 5R-1 | 5R-1 | 10R-1 | 10R-3 | 5R -1 | 7R-1 | 8R-1 | 8R-2 | 7R-1 | 1R-1 | 1R-1 | 1R-1 | 2R-1 | 2-1R | 2R-1 |
| Cm | 120-121 | 64-67 | 11-13 | 74-76 | 29.5-32 | 110-113 | 80-87 | 0-2.5 | 37-38 | 72.5-75 | 34-38 | 76-77 | 81-83 | 34-35 | 37.5-40 | 134-139 | 31-36 | 52-55 | 66-68 |
| Top depth | 1.780 | 3.360 | 0.110 | 3.420 | 7.175 | 7.980 | 15.520 | 16.290 | 6.355 | 9.713 | 11.048 | 12.268 | 10.534 | 0.340 | 0.375 | 1.340 | 2.030 | 2.240 | 2.940 |
| Bottom depth | 1.790 | 3.390 | 0.130 | 3.440 | 7.200 | 8.010 | 15.590 | 16.315 | 6.365 | 9.738 | 11.088 | 12.278 | 10.554 | 0.350 | 0.400 | 1.390 | 2.080 | 2.270 | 2.960 |
| Rock type | Serp Metadol Dunite | Metagb | Serp. Harzburgite | Serp Harzburgite | Metadol | Metadol Harzburgite | Serp Dunite | Serp | Talc schist Harzburgite | Metasom Harzburgite | Metasom Harzburgite | Metasom Harzburgite | Serp | Talc schist Harzburgite | Serp | Gabbro | Gabbro | Talc schist | |
| **Major elements (wt.%)** | | | | | | | | | | | | | | | | | | | |
| **$SiO_2$** | 36.62 | 26.21 | 37.75 | 39.95 | 26.31 | 31.61 | 36.19 | 33.08 | 50.64 | 42.41 | 38.60 | 43.53 | 39.55 | 50.01 | 40.03 | 52.14 | 50.77 | 59.63 | 47.09 |
| **$TiO_2$** | 0.02 | 0.24 | 0.02 | 0.05 | 0.92 | 1.40 | 0.03 | 0.03 | 0.14 | 0.03 | 0.03 | 0.05 | 0.03 | 0.10 | 0.03 | 0.43 | 0.30 | 0.02 | 1.08 |
| **$Al_2O_3$** | 1.11 | 21.04 | 1.17 | 1.27 | 18.48 | 20.36 | 1.02 | 1.58 | 3.82 | 1.05 | 1.22 | 1.86 | 0.86 | 4.27 | 1.16 | 16.40 | 17.53 | 1.05 | 18.23 |
| **$Fe_2O_3$** | 9.06 | 32.07 | 9.19 | 9.34 | 27.46 | 18.75 | 8.85 | 10.98 | 3.35 | 9.79 | 9.91 | 6.92 | 8.24 | 8.49 | 9.98 | 8.30 | 6.75 | 6.68 | 12.09 |
| **MnO** | 0.08 | 0.68 | 0.11 | 0.10 | 0.17 | 0.16 | 0.08 | 0.07 | 0.06 | 0.09 | 0.09 | 0.13 | 0.20 | 0.14 | 0.11 | 0.15 | 0.13 | 0.14 | 0.12 |
| **MgO** | 40.05 | 14.19 | 39.58 | 39.49 | 16.68 | 17.41 | 37.71 | 39.22 | 26.06 | 37.03 | 37.61 | 33.18 | 37.86 | 22.87 | 38.78 | 9.25 | 8.98 | 28.14 | 11.23 |
| **CaO** | 0.09 | 0.40 | 0.10 | 0.27 | 1.06 | 3.58 | 1.75 | 0.18 | 7.66 | 0.72 | 0.45 | 2.26 | 1.03 | 2.64 | 0.25 | 11.62 | 11.27 | 1.66 | 7.90 |
| **$Na_2O$** | 0.00 | 0.28 | 0.00 | 0.10 | 0.14 | 0.66 | 0.09 | 0.00 | 0.21 | 0.15 | 0.09 | 0.35 | 0.14 | 0.26 | 0.15 | 2.82 | 2.75 | 0.22 | 1.88 |
| **$K_2O$** | 0.00 | 0.03 | 0.00 | 0.05 | 0.00 | 0.02 | 0.00 | 0.00 | 0.00 | 0.00 | 0.00 | 0.00 | 0.01 | 0.00 | 0.05 | 0.00 | 0.00 | 0.02 | 0.00 |
| **$P_2O_5$** | 0.01 | 0.02 | 0.02 | 0.02 | 0.06 | 0.12 | 0.00 | 0.01 | 0.02 | 0.01 | 0.00 | 0.01 | 0.02 | 0.04 | 0.00 | 0.04 | 0.01 | 0.01 | 0.07 |
| **LOI** | 12.10 | 8.49 | 11.82 | 12.06 | 8.31 | 7.86 | 13.58 | 13.81 | 4.73 | 10.82 | 12.38 | 10.27 | 12.97 | 5.34 | 11.95 | 0.41 | 0.30 | 4.30 | 3.33 |
| **TOTAL** | 99.14 103.02 | 103.63 | 99.76 | 102.70 | 99.59 | 101.92 | 99.29 | 98.95 | 96.70 | 102.10 | 100.38 | 98.55 | 100.91 | 94.16 | 102.47 | 101.57 | 98.80 | 101.86 | |
| Mg# | 90 | 47 | 90 | 89 | 55 | 65 | 89 | 88 | 94 | 88 | 88 | 90 | 90 | 84 | 89 | 69 | 73 | 89 | 65 |
| $MgO/SiO_2$ | 1.09 | 0.54 | 1.05 | 0.99 | 0.63 | 0.55 | 1.04 | 1.19 | 0.51 | 0.87 | 0.97 | 0.76 | 0.96 | 0.46 | 0.97 | 0.18 | 0.18 | 0.47 | 0.24 |
| $Al_2O_3/SiO_2$ | 0.03 | 0.80 | 0.03 | 0.03 | 0.70 | 0.64 | 0.03 | 0.05 | 0.08 | 0.02 | 0.03 | 0.04 | 0.02 | 0.09 | 0.03 | 0.31 | 0.35 | 0.02 | 0.39 |
| **Trace elements (ppm)** | | | | | | | | | | | | | | | | | | | |
| **Cr** | 21572 | 748 | 11705 | 3796 | 680 | 523 | 8363 | 29698 | 1986 | 2746 | 3614 | 2663 | 2420 | 1349 | 3079 | 100 | 142 | 1746 | 414 |
| **Ni** | 14590 | 190 | 6715 | 2987 | 341 | 436 | 6531 | 7931 | 1253 | 3687 | 2193 | 1984 | 2810 | 1640 | 1651 | 97 | 94 | 1741 | 226 |
| **Li** | 22.74 | 16.60 | 12.95 | 3.93 | 6.76 | 12.76 | 2.59 | 0.22 | 0.15 | 1.47 | 0.49 | 1.94 | 8.73 | 13.12 | 6.29 | 5.65 | 4.39 | 21.67 | 12.48 |
| **Sc** | 82.79 | 41.08 | 30.04 | 16.53 | 37.40 | 41.16 | 29.24 | 14.31 | 17.68 | 9.71 | 6.60 | 8.35 | 7.95 | 7.91 | 10.37 | 41.62 | 35.61 | 7.56 | 35.90 |
| **V** | 340 | 139 | 190 | 74 | 198 | 292 | 85 | 116 | 60 | 28 | 26 | 32 | 34 | 29 | 42 | 190 | 151 | 19 | 179 |
| **Co** | 622 | 152 | 315 | 137 | 191 | 149 | 282 | 408 | 33 | 155 | 101 | 77 | 116 | 78 | 95 | 38 | 35 | 56 | 53 |
| **Cu** | 120 | 0 | 231 | 16 | 0 | 1 | 5 | 14 | 3 | 1 | 0 | 1 | 4 | 18 | 24 | 49 | 44 | 18 | 2 |
| **Zn** | 318 | 331 | 395 | 64 | 44 | 38 | 88 | 255 | 7 | 21 | 21 | 16 | 24 | 73 | 57 | 48 | 39 | 87 | 24 |
| **Ga** | 9.62 | 10.49 | 5.55 | 1.58 | 18.54 | 23.42 | 2.96 | 7.10 | 5.56 | 2.13 | 1.74 | 3.17 | 1.23 | 7.34 | 1.21 | 14.86 | 14.46 | 2.03 | 17.29 |
| **Rb** | 0.20 | 0.16 | 0.10 | 0.03 | 0.07 | 0.13 | 0.00 | 0.00 | 0.00 | 0.10 | 0.05 | 0.31 | 0.07 | 0.11 | 0.13 | 0.36 | 0.16 | 0.11 | 0.27 |
| **Sr** | 17.24 | 3.01 | 10.09 | 3.06 | 1.73 | 57.97 | 757.58 | 3.61 | 2.72 | 2.13 | 1.02 | 3.01 | 13.60 | 3.96 | 3.29 | 81.98 | 84.97 | 2.36 | 72.47 |
| **Y** | 2.33 | 6.88 | 0.99 | 0.38 | 22.71 | 31.68 | 2.18 | 0.09 | 7.15 | 3.54 | 1.84 | 7.12 | 2.12 | 41.57 | 1.03 | 14.84 | 8.08 | 0.43 | 27.57 |
| **Zr** | 0.00 | 3.13 | 0.00 | 0.09 | 23.45 | 20.82 | 1.23 | 0.00 | 4.11 | 1.54 | 1.17 | 5.11 | 0.38 | 5.43 | 0.33 | 17.45 | 4.76 | 0.41 | 39.78 |
| **Nb** | 0.11 | 0.02 | 0.02 | 0.02 | 0.35 | 1.56 | 0.05 | 0.05 | 0.15 | 0.49 | 0.47 | 0.51 | 0.03 | 1.89 | 0.06 | 0.30 | 0.05 | 0.05 | 1.24 |
| **Mo** | 2.18 | 0.22 | 1.04 | 0.27 | 0.21 | 0.14 | 0.62 | 0.37 | 0.01 | 0.21 | 0.18 | 0.21 | 1.30 | 0.46 | 0.40 | 0.16 | 0.20 | 0.15 | 0.18 |
| **Cd** | 95.23 | 40.86 | 33.98 | 26.71 | 8.63 | 16.64 | 17.48 | 15.49 | 4.10 | 6.83 | 6.43 | 10.01 | 49.11 | 29.42 | 27.48 | 62.06 | 35.36 | 9.30 | 20.17 |
| **Sn** | 0.05 | 1.71 | 0.20 | 0.08 | 0.55 | 0.81 | 0.20 | 0.14 | 0.22 | 0.23 | 0.28 | 0.53 | 0.10 | 1.28 | 0.82 | 1.16 | 0.26 | 0.37 | 0.83 |
| **Sb** | 1.09 | 0.02 | 1.34 | 0.15 | 0.01 | 0.00 | 0.01 | 0.01 | 0.00 | 0.00 | 0.00 | 0.02 | 0.13 | 0.05 | 0.29 | 0.03 | 0.02 | 0.03 | 0.01 |
| **Ba** | 1.19 | 0.17 | 0.97 | 0.30 | 0.20 | 1.33 | 0.72 | 0.00 | 0.00 | 0.00 | 0.15 | 0.16 | 4.58 | 0.87 | 0.88 | 4.41 | 2.15 | 0.23 | 2.32 |
| **La** | 0.16 | 0.30 | 0.18 | 0.00 | 0.85 | 3.05 | 0.23 | 0.00 | 0.21 | 0.47 | 0.24 | 0.57 | 0.13 | 8.56 | 0.30 | 0.92 | 0.26 | 0.09 | 1.55 |
| **Ce** | 0.33 | 0.72 | 0.05 | 0.00 | 2.69 | 10.48 | 0.74 | 0.02 | 1.06 | 1.72 | 0.90 | 2.33 | 0.29 | 30.19 | 1.32 | 3.29 | 0.84 | 0.28 | 5.82 |
| **Nd** | 0.40 | 1.05 | 0.22 | 0.01 | 3.81 | 9.26 | 0.60 | 0.03 | 1.56 | 1.23 | 0.75 | 2.20 | 0.49 | 16.89 | 0.61 | 3.21 | 1.15 | 0.15 | 6.44 |
| **Sm** | 0.17 | 0.54 | 0.05 | 0.00 | 1.92 | 3.33 | 0.17 | 0.01 | 0.68 | 0.34 | 0.22 | 0.72 | 0.15 | 4.43 | 0.16 | 1.28 | 0.58 | 0.04 | 2.53 |
| **Eu** | 0.10 | 0.41 | 0.05 | 0.02 | 0.24 | 0.96 | 0.11 | 0.01 | 0.26 | 0.10 | 0.06 | 0.19 | 0.07 | 0.52 | 0.25 | 0.63 | 0.45 | 0.04 | 0.95 |
| **Gd** | 0.33 | 0.80 | 0.08 | 0.00 | 2.57 | 4.09 | 0.23 | 0.00 | 0.89 | 0.40 | 0.24 | 0.85 | 0.20 | 4.86 | 0.17 | 1.72 | 0.86 | 0.05 | 3.23 |
| **U** | 5.05 | 0.01 | 3.27 | 1.52 | 0.02 | 0.06 | 2.22 | 4.50 | 0.02 | 0.16 | 0.03 | 1.19 | 1.98 | 0.09 | 0.47 | 0.04 | 0.01 | 0.06 | 0.02 |

Notes:
Depths are given as meters below surface (mbsf).
Abbreviations: LOI = Loss on Ignition; Serpentinized: Serp; Metagb: metagabbro; Metasom: metasomatic overprinting
Mg# = Mg/(Mg + Fe)*100. Note: Mg#s published in Früh-Green et al., 2017a are incorrect. These have been recalculated here from the oxide weight %, assuming the atomic ratio of 100 x Mg/(Mg + $Fe^{2+}$), using molecular weights and a factor of 0.8998 to calculate $Fe^{2+}$ from $Fe_2O_3$.

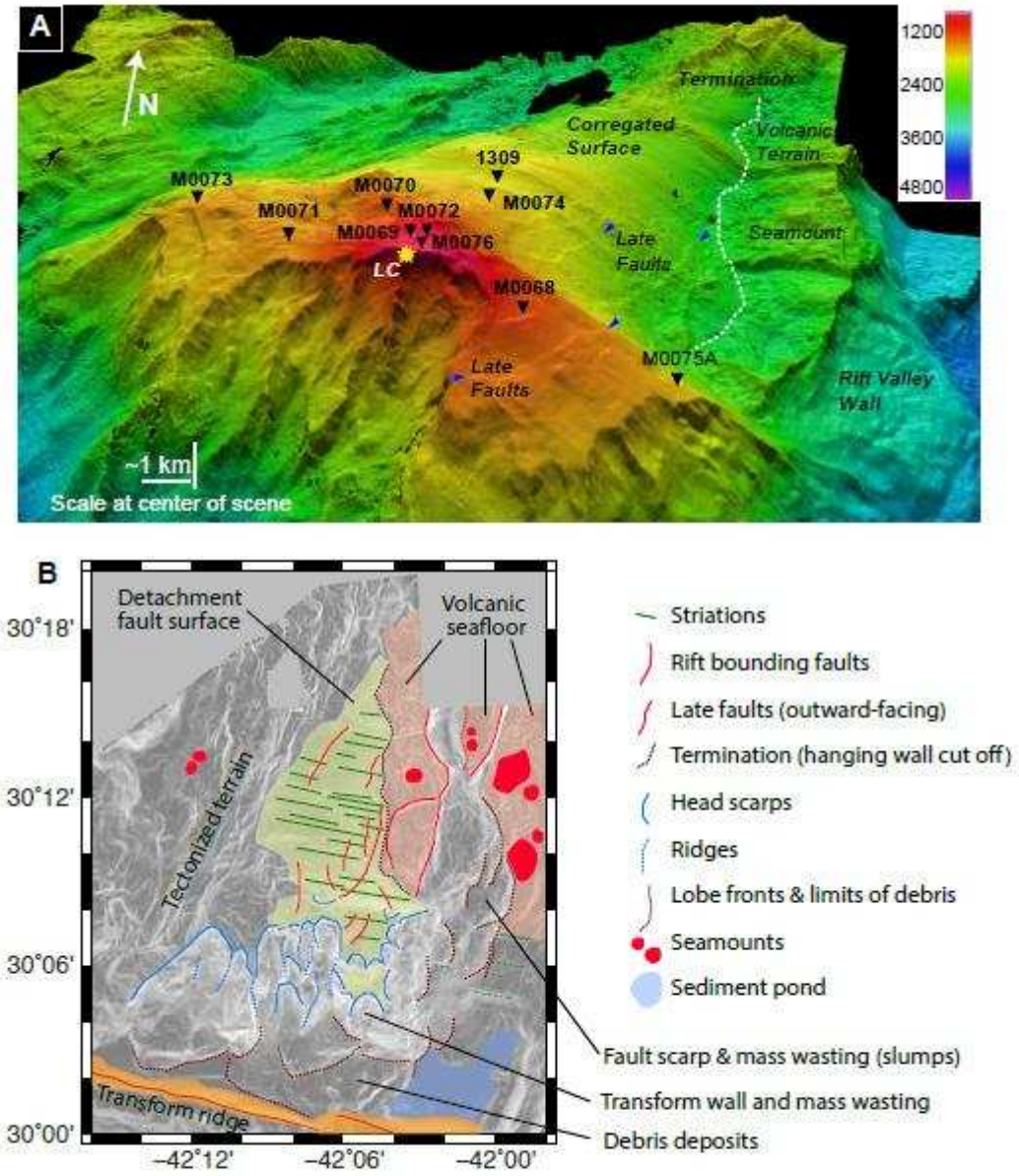


Figure 1. Bathymetry together with structural and morphological characteristics of the Atlantis Massif. (a) 3-D terrain model with a northward view of the detachment fault surface showing striations associated with detachment faulting, cross-cutting tectonic structures, with locations of the IODP Expedition 357 drill sites, the Lost City hydrothermal field (LC, yellow star) and IODP Site U1309. Based on new multibeam bathymetry acquired at 50 m resolution. (b) Interpretation of structural and morphological characteristics from new bathymetry data acquired during the expedition (reproduced from Früh-Green et al., 2017a).

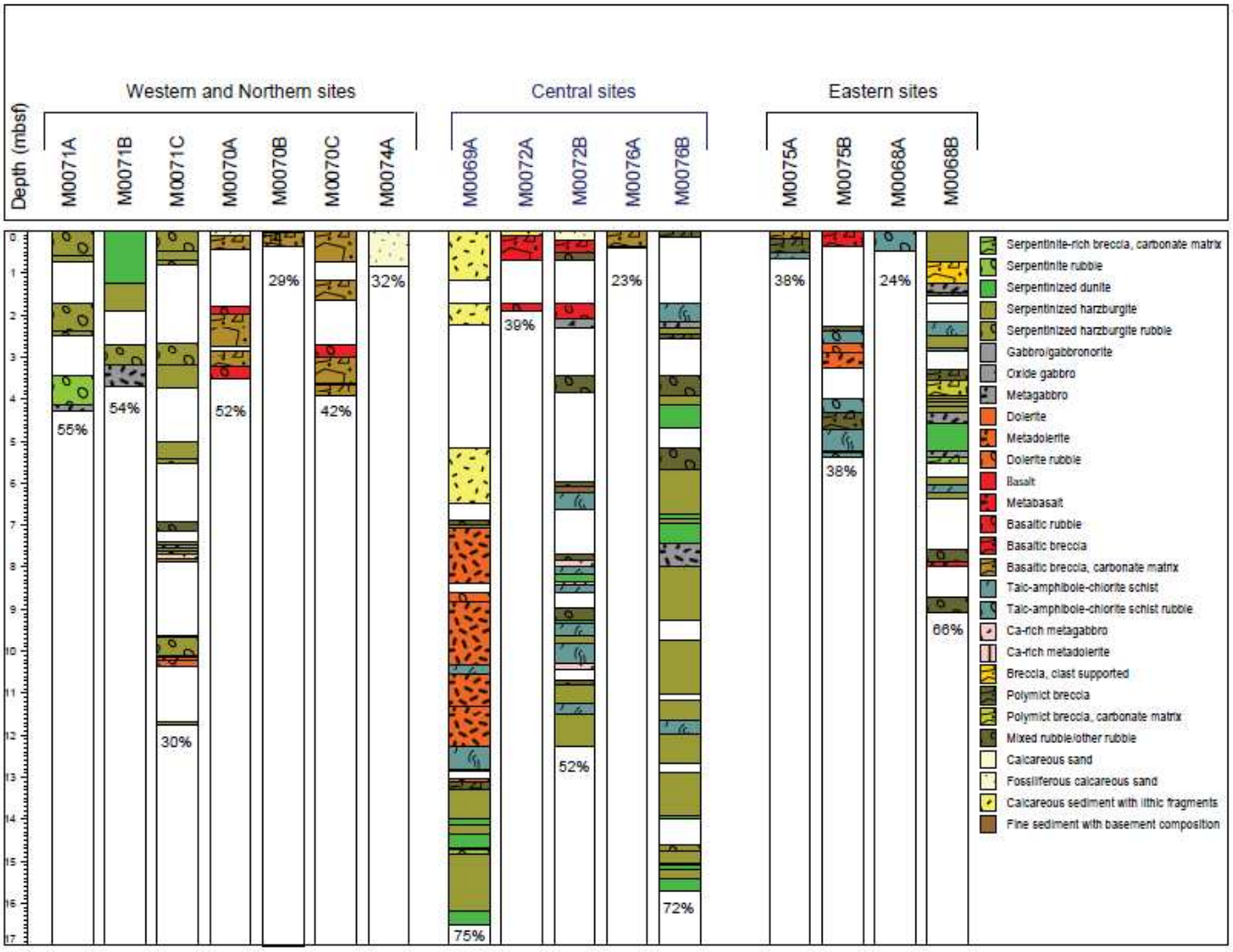


Figure 2. Lithologic variations on a regional scale and with depth in cores recovered during IODP Expedition 357. Percentages indicate overall percent core recovery for each hole. The central sites, highlighted in blue, recovered in situ sequences, whereas talus debris was recovered at the western and eastern sites along the southern ridge.

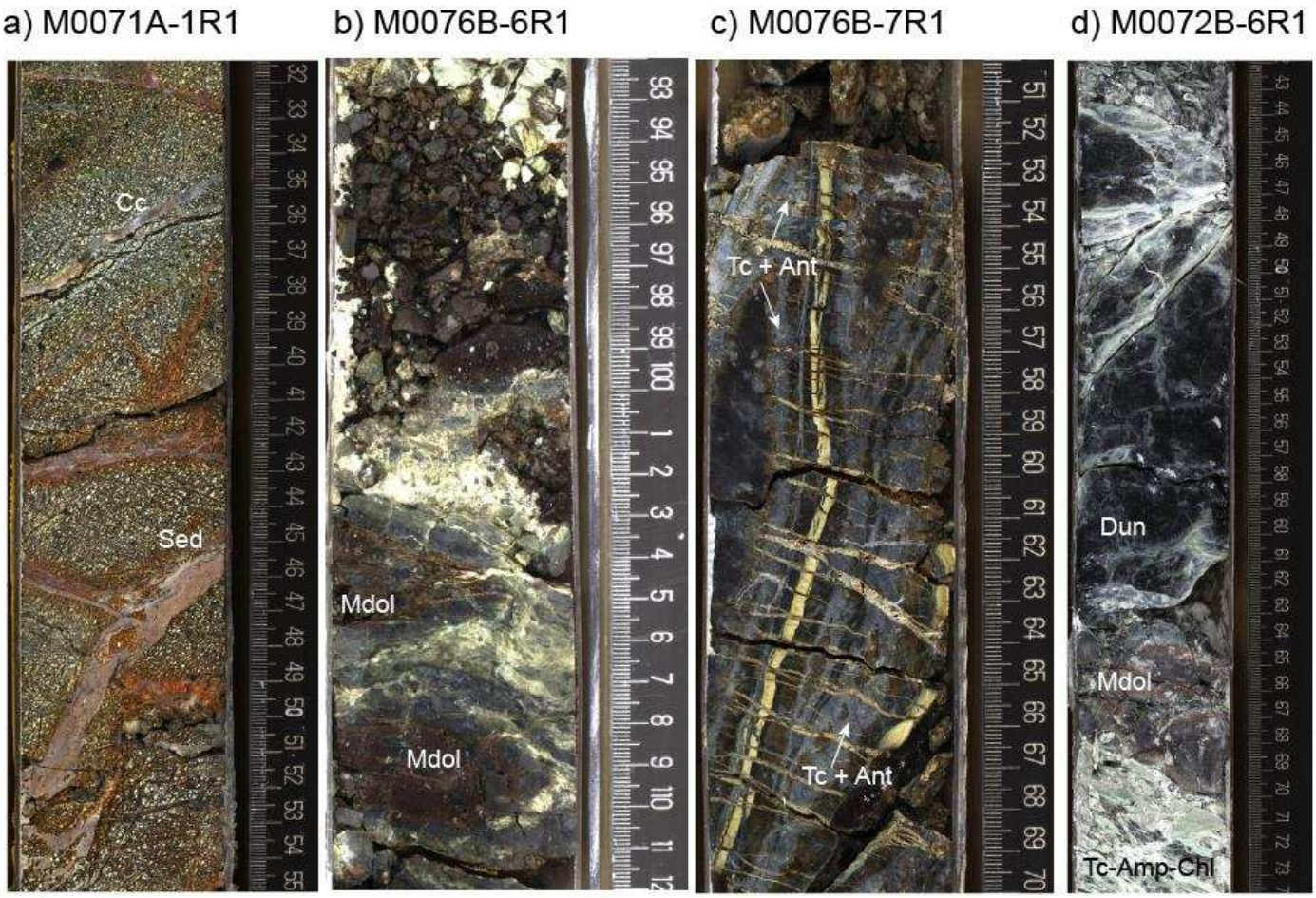


Figure 3. Examples of variations in rock type and structures in IODP Exp. 357 drill cores. (a) Serpentinized and oxidized dunite cut by moderately dipping calcite veins (Cc) and fractures filled with foraminiferous carbonate sediment (Sed). (b) Relationships between schistose zone talc-amphibole-chlorite schists (greenish-white domains) at the contact to cataclastically deformed metadolerite (Mdol). (c) Steeply dipping banded serpentine ± talc veins cutting serpentinized harzburgite. Light grey domains are previous fluid pathways resulting in metasomatic replacement of antigorite (Ant) by talc (Tc) (Rouméjon et al., 2018). (d) Metasomatic zones of talc-amphibole-chlorite schist (Tc-Amp-Chl) at contact to serpentinized dunite (Dun) intruded by dolerite and transitioning again to talc-amphibole-chlorite schist. Photos: IODP ESO.

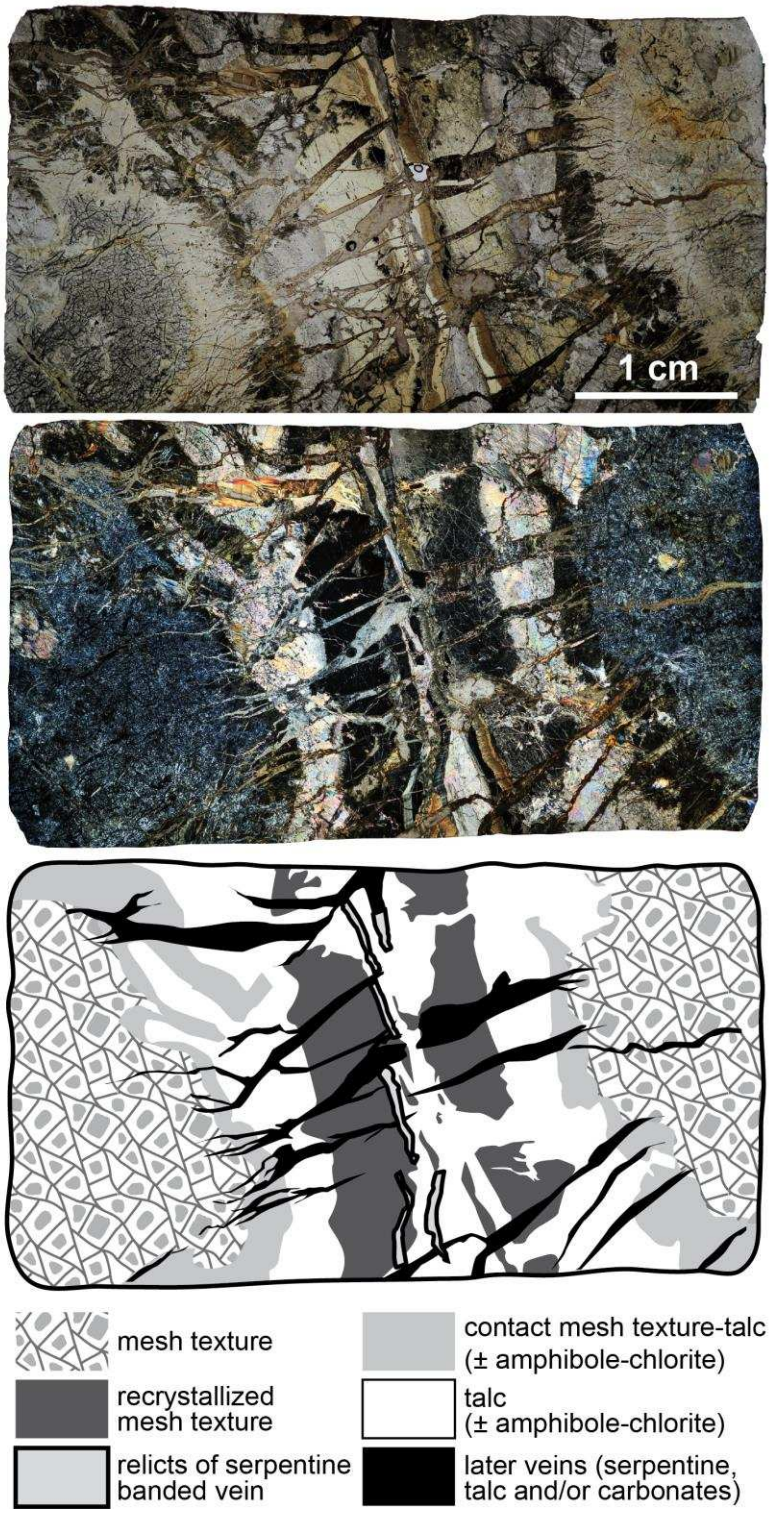


Figure 4. Characteristic serpentine textures and cross-cutting relationships associated with progressive alteration and veining in serpentinized harburzgite (example from M0076B-7R1, 43-45cm); (a) plane polarized light, (b) crossed polarized light, and (c) schematic representation of overprinting relationships. Modified from Früh-Green et al., 2017d, Fig. 7.

Figure 5

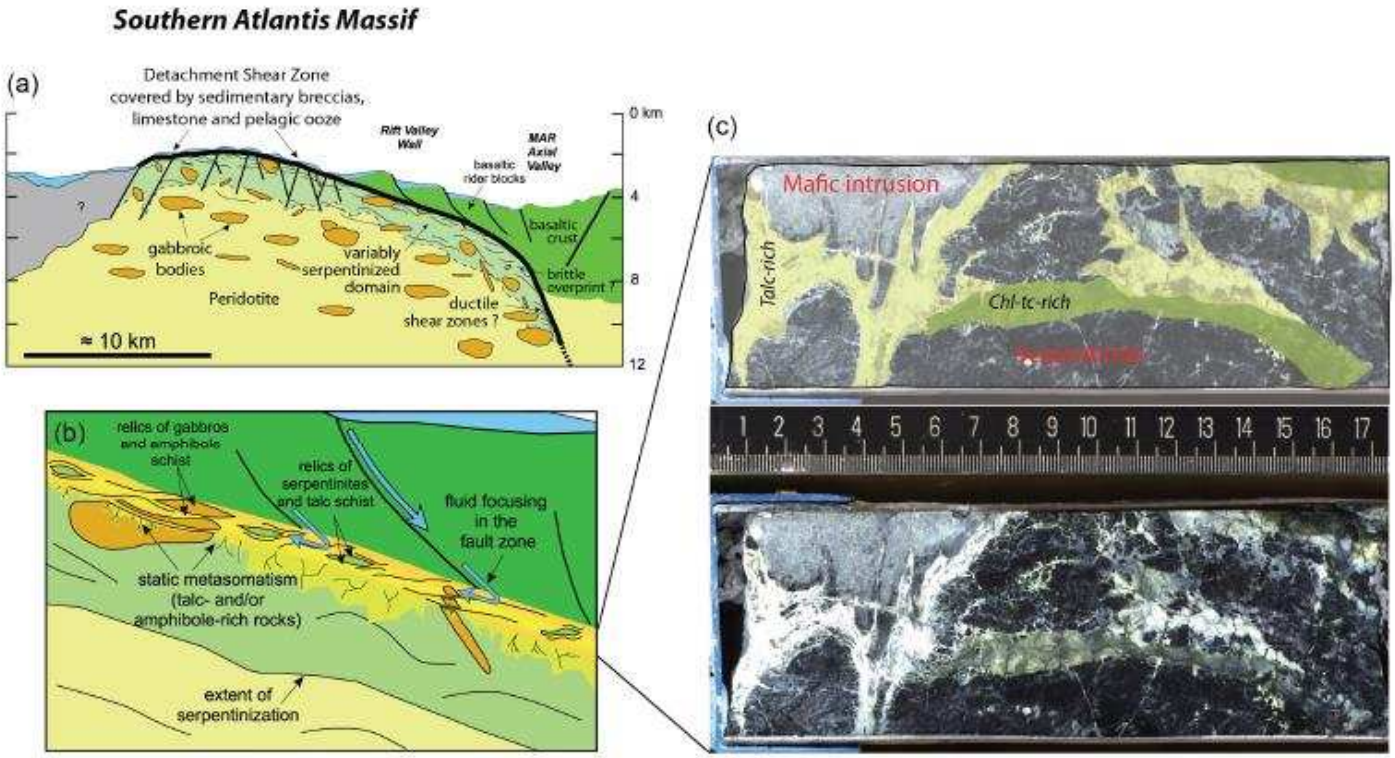


Figure 5. Model of the tectono-magmatic evolution and alteration of heterogeneous lithosphere at Atlantis Massif. (a) Interpretative cross section showing fluid pathways, metasomatic zones and extent of serpentinization (light green shaded region) related to detachment faulting and steep normal faults (modified after Boschi et al., 2006a). (b) Detail of <100 m detachment shear zone (in red-yellow) characterized by heterogeneous, variably altered and deformed gabbroic and peridotite lithologies and with extensive synkinematic metasomatism. The resulting talc-amphibole schists enclose lenses of relic, locally less deformed, serpentinite and gabbroic rocks (modified from Boschi et al., 2006a). (c) Example of magmatic intrusion in a fully serpentinized harzburgite from Core M0072-8R2, 0–18 cm. Late metasomatic alteration at the contact between the mafic/ultramafic rocks produced white and green talc-amphibole-chlorite assemblages that crosscut the previous texture. Chl = chlorite, tc = talc (reproduced from Früh-Green et al., 2017d, Fig. 13).

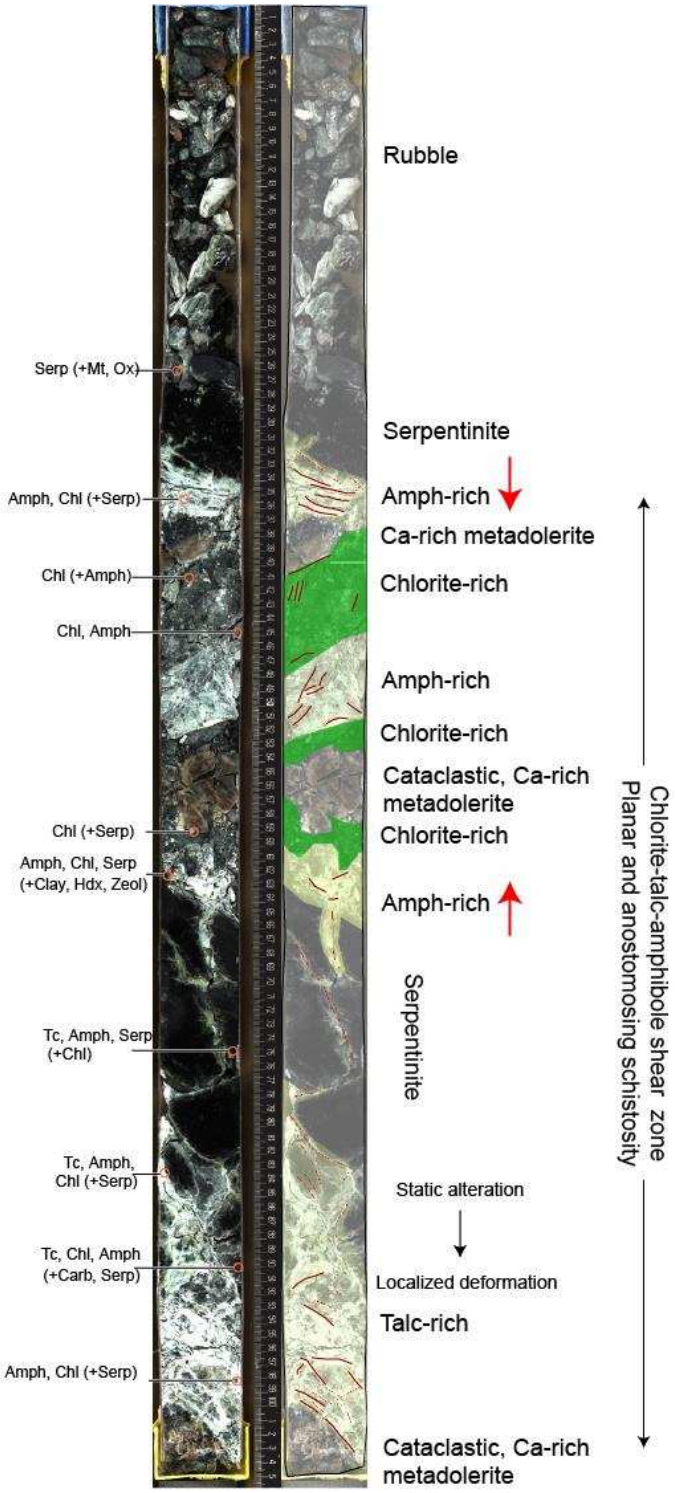


Figure 6. Example of complex lithological and deformation relationships between mafic intrusions in peridotite and metasomatic domains in the IODP Expedition 357 cores, showing a transition from static alteration to strain localization in alternating talc-, amphibole-, and chlorite-rich shear zones (from Core M0072B-7R-1, 0–105 cm). Red circles = samples taken for XRD analyses and corresponding mineral assemblages. Serp = serpentinite, Mt = magnetite, Ox = oxide, Amph = amphibole, Chl = chlorite, Hdx = hydroxide, Zeol = zeolite, Carb = carbonate. Modified from Früh-Green et al., 2017d, Fig. 12.

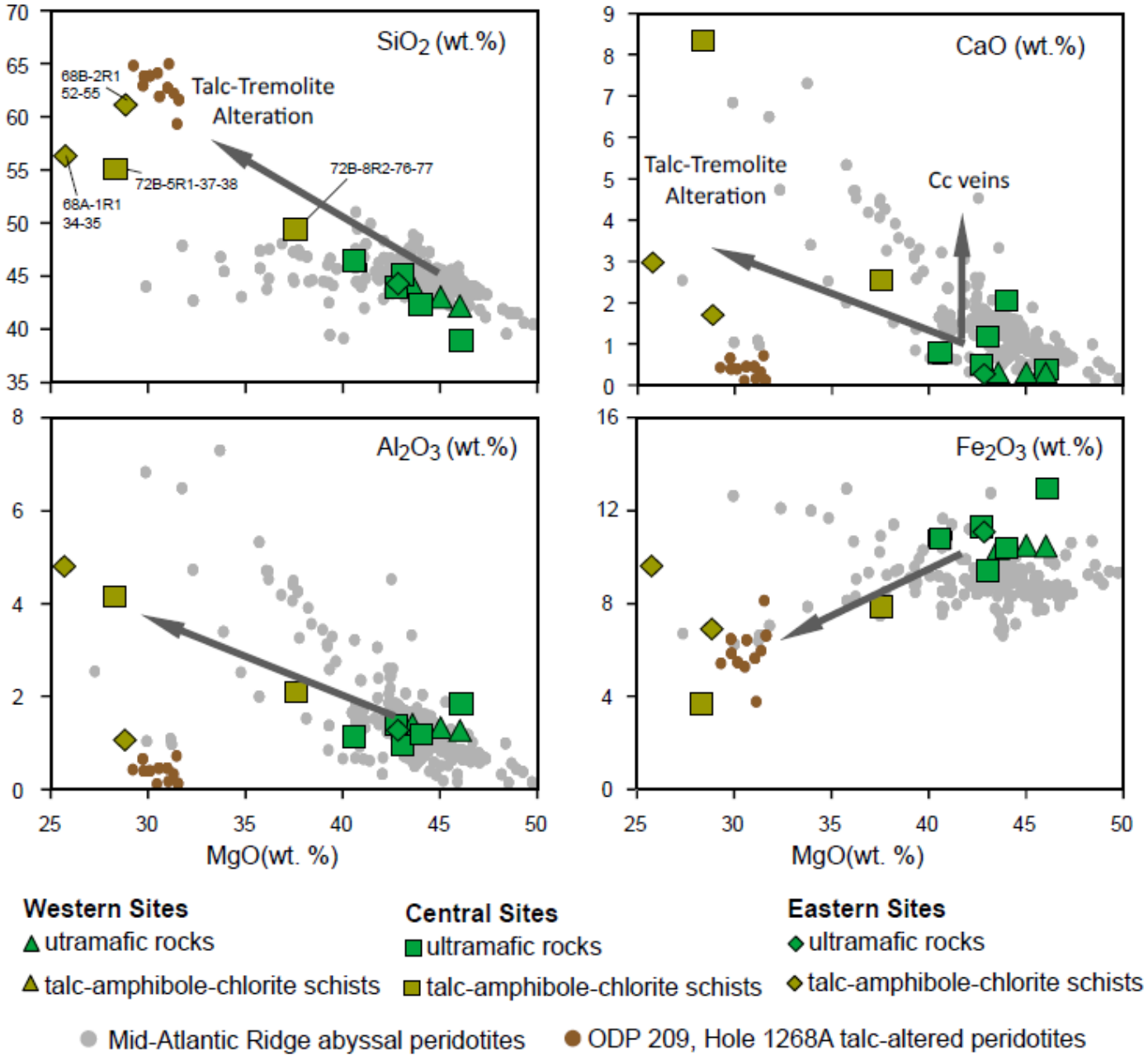


Figure 7. Selected whole-rock major elements (normalized, volatile-free compositions, and in weight % oxides, wt %) vs. MgO for serpentinized ultramafic rocks (including impregnated / metasomatized samples) and talc-amphibole-chlorite schists from Atlantis Massif, IODP Exp. 357. Data from Mid-Atlantic-Ridge abyssal serpentinized peridotites and talc-altered peridotites are shown for comparison. Talc-amphibole alteration is associated with a general trend to higher Si, Ca and Al compositions and a decrease in Mg and Fe. Global abyssal peridotite field defined by data from PetDB (http://www.earthchem.org/petdb, May 2016). Data for talc-altered peridotite field from ODP Leg 209, Hole 1268A (Paulick et al., 2006; also from PetDB). Modified from Früh-Green et al., 2017a, Fig. 11.

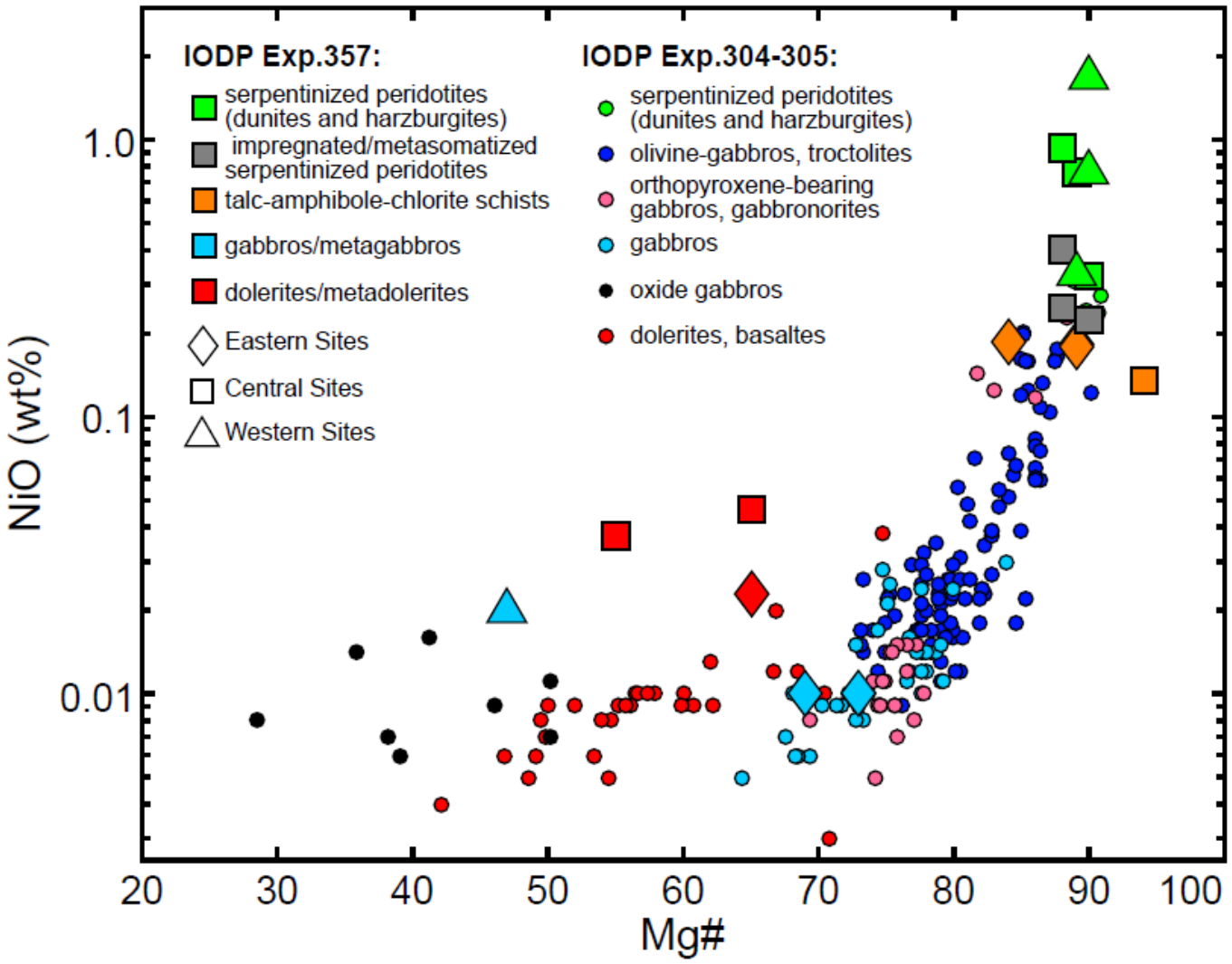


Figure 8. Ni concentrations (calculated as weight % (wt %) oxides and normalized to volatile-free concentrations, plotted on a log scale) vs. Mg# of Atlantis Massif mafic and ultramafic rocks from Expedition 357 compared with those from cores recovered at Site U1309 during Integrated Ocean Drilling Program Expedition 304/305 (Godard et al., 2009).

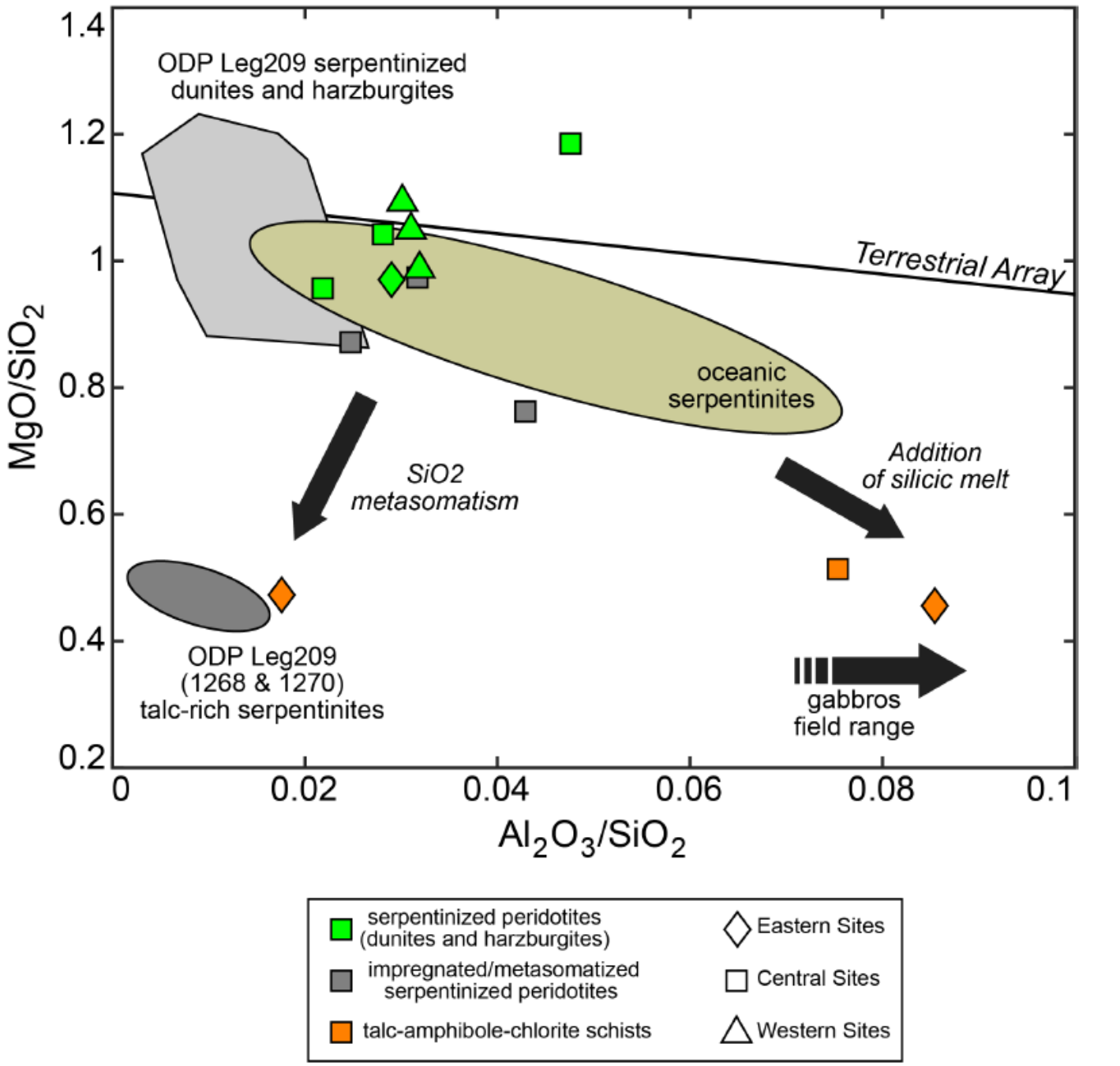


Figure 9. $MgO/SiO_2$ vs $Al_2O_3/SiO_2$ diagram showing variations in bulk rock chemistry and changes with Si-metasomatism. Atlantis Massif compositions are also compared with compositions of serpentinites and talc schists from IODP Site U1309 and from 15°20′N recovered during ODP Leg 209 (Paulick et al., 2006) as well as the global data set of abyssal peridotites reported in Niu (2004), which define a trend parallel to the terrestrial array (Jagoutz et al., 1979). The geochemistry of the Atlantis Massif samples reflects a variety of processes including modal mineralogical composition, melt impregation and multiple phases of hydrothermal alteration.

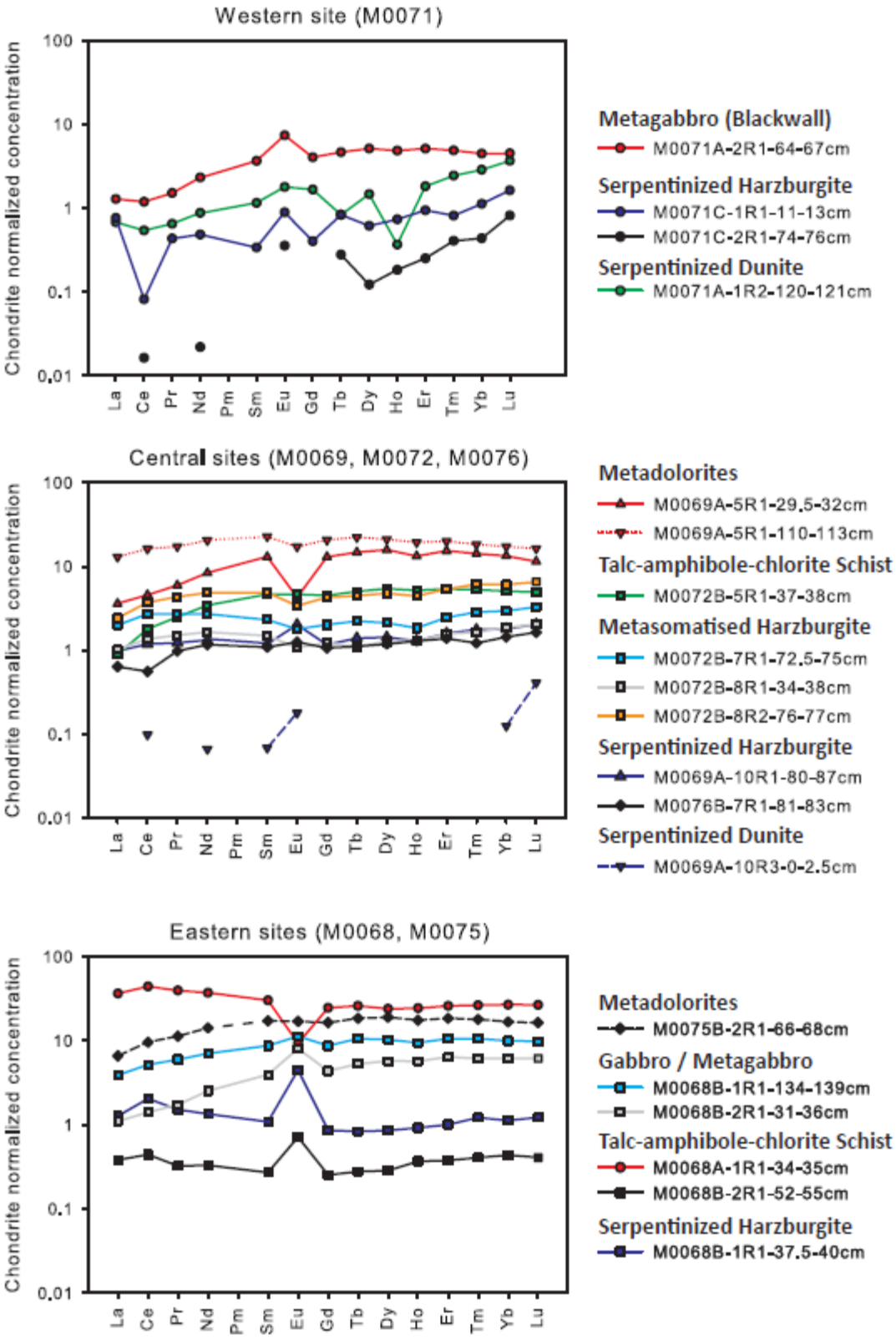


Figure 10. Compilation of chondrite-normalized REE concentrations of Atlantis Massif mafic and ultramafic rocks from samples of the IODP Expedtion 357 drill cores (see Table 2). Values for CI chondrite from McDonough and Sun, 1995.

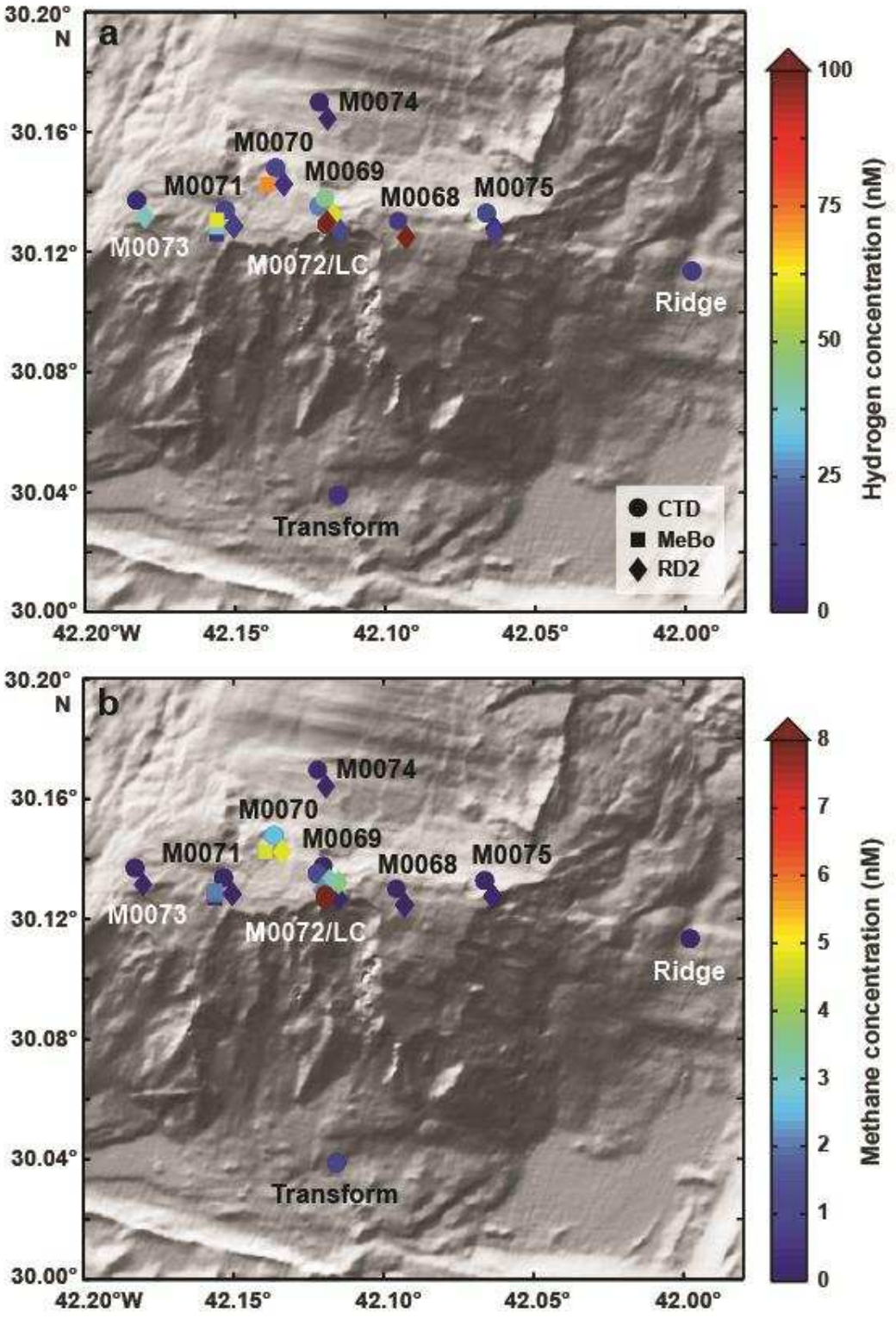


Figure 11. Highest measured hydrogen and methane concentrations in samples from CTD rosette bottom waters acquired before drilling and sensor package Niskin bottles taken by RD2 and MeBo after drilling at the Atlantis Massif drill sites during IODP Expedition 357. Dark red circles indicate samples from the Lost City (LC) plume.

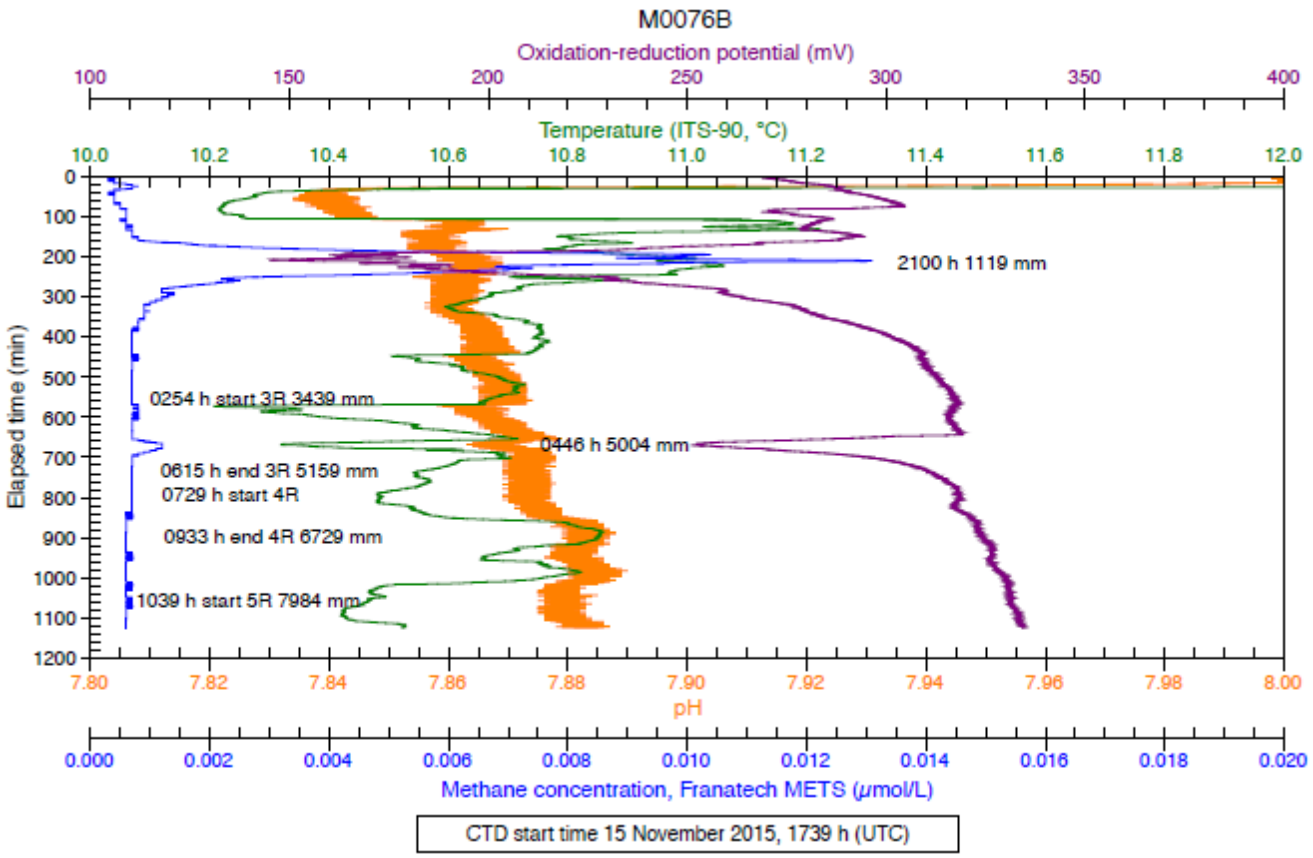


Figure 12. Example of variations in fluid chemistry during drilling operations and correlations of geochemical signatures recorded by the sensor packages on the rock drills from sensor data for Hole M0076B, Cores 1R–5R. Elapsed time = time since the start of the sensor package data file. Penetration depth (in mm) was reconstructed from drill logs.

Figure 13. Frame-grab photograph from drilling video of bubbles (black arrows) that were observed issuing from Hole M0070C and around the drill base during operations at this site, even when coring had stopped.

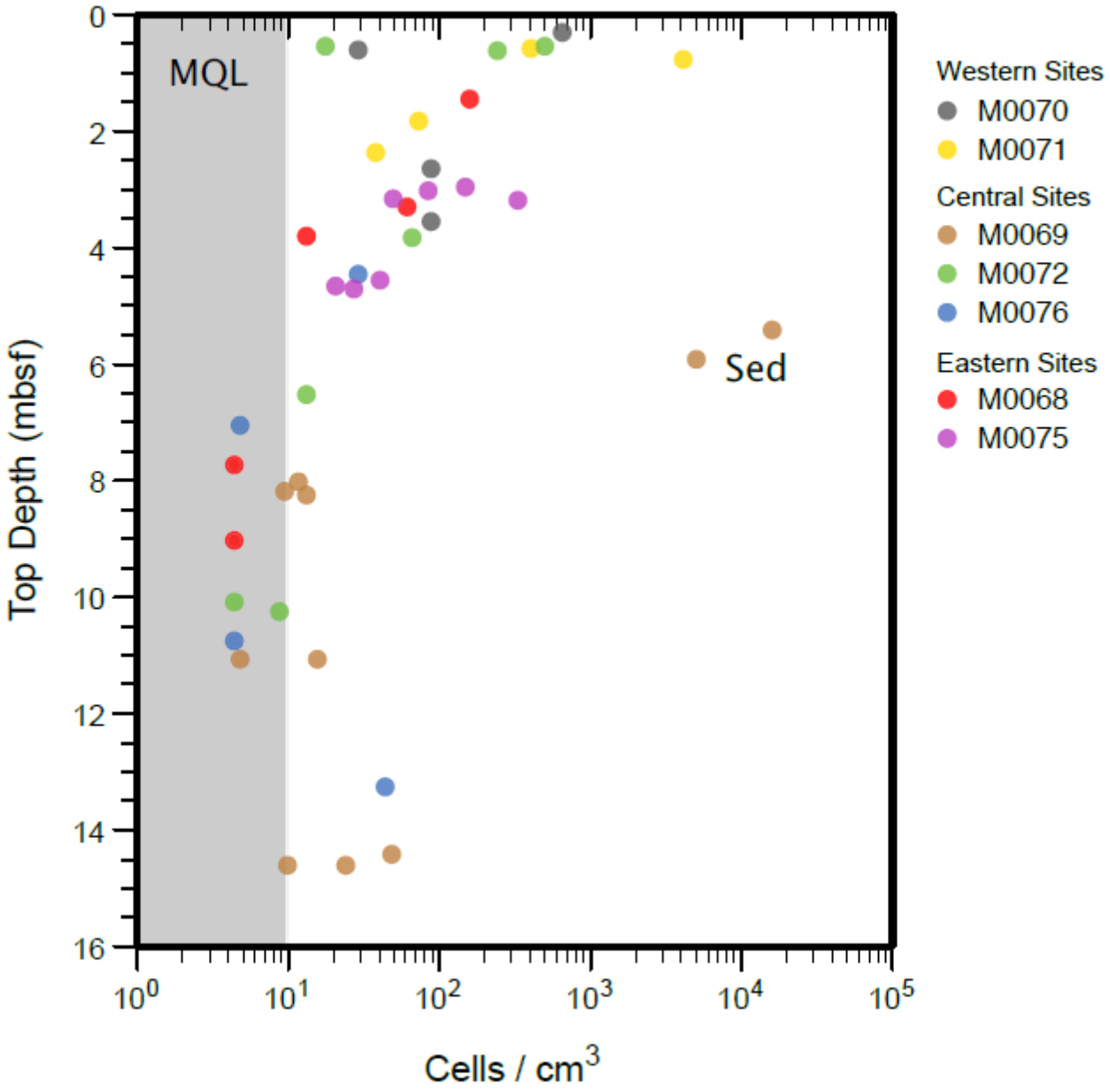


Figure 14. Downhole variations in cell counts from interior portions of whole round cores of the basement rock samples (and two sediment (Sed) samples from Hole M0069A) taken onboard during IODP Exp. 357. Data from Hole M0074 not included due to extensive damage to this short sediment core. The shaded region shows the range of counts below the minimum quantification limit (MQL) of 9.8 cells $cm^{-3}$.